PHYSICAL REVIEW D **79,** 124032 (2009)

# Constraints on a phenomenologically parametrized neutron-star equation of state

Jocelyn S. Read,[1] Benjamin D. Lackey,[1] Benjamin J. Owen,[2] and John L. Friedman[1]

[1]*Department of Physics, University of Wisconsin-Milwaukee, P.O. Box 413, Milwaukee, Wisconsin 53201, USA*

[2]*Center for Gravitational Wave Physics, Institute for Gravitation and the Cosmos, and Department of Physics, The Pennsylvania State University, University Park, Pennsylvania 16802-6300, USA*

(Received 22 January 2009; published 22 June 2009)

We introduce a parametrized high-density equation of state (EOS) in order to systematize the study of constraints placed by astrophysical observations on the nature of neutron-star matter. To obtain useful constraints, the number of parameters must be smaller than the number of EOS-related neutron-star properties measured, but large enough to accurately approximate the large set of candidate EOSs. We find that a parametrized EOS based on piecewise polytropes with 3 free parameters matches, to about 4% rms error, an extensive set of candidate EOSs at densities below the central density of $1.4M_{\odot}$ stars. Adding observations of more massive stars constrains the higher-density part of the EOS and requires an additional parameter. We obtain constraints on the allowed parameter space set by causality and by present and near-future astronomical observations with the least model dependence. Stringent constraints on the EOS parameter space are associated with the future measurement of the moment of inertia of PSR J0737-3039A combined with the maximum known neutron-star mass. We also present in an appendix a more efficient algorithm than has previously been used for finding points of marginal stability and the maximum angular velocity of stable stars.

DOI: 10.1103/PhysRevD.79.124032 PACS numbers: 04.40.Dg, 26.60.Kp, 97.60.Jd

## I. INTRODUCTION

Because the temperature of neutron stars is far below the Fermi energy of their constituent particles, neutron-star matter is accurately described by the one-parameter equation of state (EOS) that governs cold matter above nuclear density. The uncertainty in that EOS, however, is notoriously large, with the pressure $p$ as a function of baryon mass density $\rho$ uncertain by as much as an order of magnitude above nuclear density. The phase of the matter in the core of a neutron star is similarly uncertain: Current candidates for the EOS include nonrelativistic and relativistic mean-field models; models for which neutron-star cores are dominated by nucleons, by hyperons, by pion or kaon condensates, and by strange quark matter (free up, down, and strange quarks); and one cannot yet rule out the possibility that the ground state of cold matter at zero pressure might be strange quark matter and that the term ''neutron star'' is a misnomer for strange quark stars.

The correspondingly large number of fundamental parameters needed to accommodate the models' Lagrangians has meant that studies of astrophysical constraints (see, for example, [1–5] and references therein) present constraints by dividing the EOS candidates into an allowed and a ruled-out list. A more systematic study, in which astrophysical constraints are described as constraints on the parameter space of a parametrized EOS, can be effective only if the number of parameters is smaller than the number of neutron-star properties that have been measured or will have been measured in the next several years. At the same time, the number of parameters must be large enough to accurately approximate the EOS candidates.

A principal aim of this paper is to show that, if one uses phenomenological rather than fundamental parameters, one can obtain a parametrized EOS that meets these conditions. We exhibit a parametrized EOS, based on specifying the stiffness of the star in three density intervals, measured by the adiabatic index $\Gamma = d\log p/d\log\rho$. A fourth parameter translates the $p(\rho)$ curve up or down, adding a constant pressure—equivalently fixing the pressure at the endpoint of the first density interval. Finally, the EOS is matched below nuclear density to the (presumed known) EOS. An EOS for which $\Gamma$ is constant is a polytrope, and the parametrized EOS is then piecewise polytropic. A similar piecewise-polytropic EOS was previously considered by Vuille and Ipser [6]; and, with different motivation, several other authors [7–10] have used piecewise polytropes to approximate neutron-star EOS candidates. In contrast to this previous work, we use a small number of parameters chosen to fit a wide variety of fundamental EOSs. (We take a set of 34 candidate EOSs, described below, which is an expansion of the set used in [5] and includes a variety of high-density exotic compositions as well as standard nuclear matter.) Also, we systematically explore a variety of astrophysical constraints. Like most of the previous work, we aim to model equations of state containing nuclear matter (possibly with various phase transitions) rather than pure quark stars, whose EOS is predicted to be substantially different.

As we have noted, enough uncertainty remains in the pressure at nuclear density, that one cannot simply match to a fiducial pressure at $\rho_{\mathrm{nuc}}$. Instead of taking as one parameter the pressure at a fiducial density, however, one could match to the pressure of the known subnuclear EOS

 © 2009 The American Physical Society

at, say, 0.1 $\rho_{\rm nuc}$ and then use as one parameter a value of $\Gamma_0$ for the interval between $0.1\rho_{\rm nuc}$ and $\rho_{\rm nuc}$. Neutron-star observables are insensitive to the EOS below $\rho_{\rm nuc}$, because the fraction of mass at low density is small. But the new parameter $\Gamma_0$ would indirectly affect observables by changing the value of the pressure at and above nuclear density, for fixed values of the remaining $\Gamma_i$. By choosing instead the pressure at a fixed density $\rho_1 > \rho_{\rm nuc}$, we obtain a parameter more directly connected to physical observables. In particular, as Lattimer and Prakash [5] have pointed out, neutron-star radii are closely tied to the pressure somewhat above nuclear density, and the choice $p_1 = p(\rho_1)$ is recommended by that relation.

In general, to specify a piecewise-polytropic EOS with three density intervals above nuclear density, one needs six parameters: two dividing densities, three adiabatic indices $\Gamma_i$, and a value of the pressure at an endpoint of one of the intervals. Remarkably, however, we find (in Sec. IV) that the error in fitting the collection of EOS candidates has a clear minimum for a particular choice of dividing densities. With that choice, the parametrized EOS has three free parameters, $\Gamma_1$, $\Gamma_2$, and $p_1$, for densities below $10^{15}$ g/cm$^3$ (the density range most relevant for masses $\sim 1.4 M_\odot$), and four free parameters (an additional $\Gamma_3$) for densities between $10^{15}$ g/cm$^3$ and the central density of the maximum-mass star for each EOS.

With the parametrization in hand, we examine in Sec. V astrophysical constraints on the EOS parameter space beyond the radius-$p_1$ relation found by Lattimer and Prakash [5]. Our emphasis in this first study is on present and very near-future constraints: those associated with the largest observed neutron-star mass and spin, with a possible observation (as yet unrepeated) of neutron-star redshift, with a possible simultaneous measurement of mass and radius, and with the expected future measurement of the moment of inertia of a neutron star with known mass. (We do not consider other observables, such as those associated with glitches and cooling, which depend not only on the EOS but also on dynamics, transport coefficients, and thermodynamic derivatives. The latter quantities are generally much more uncertain than the EOS and related observables such as the stellar radius, and are always more model dependent.) A companion paper [11] will investigate constraints obtainable with gravitational-wave observations in a few years.

The constraints associated with the largest observed mass, spin, and redshift have a similar form, each restricting the parameter space to one side of a surface: For example, if we take the largest observed mass (at a 90% confidence level) to be $1.7 M_\odot$, then the allowed parameters correspond to EOSs whose maximum mass is at least $1.7 M_\odot$. We can regard $M_{\rm max}$ as a function on the 4-dimensional EOS parameter space. The subspace of EOSs for which $M_{\rm max} = 1.7 M_\odot$ is then described by a 3-dimensional surface, and constraint is a restriction to the high-mass side of the surface. Similarly, the observation of a 716 Hz pulsar restricts the EOS parameter space to one side of a surface that describes EOSs for which the maximum spin is 716 Hz. Thus we can produce model-independent extended versions of the multidimensional constraints seen in [12].

The potential simultaneous observation of two properties of a single neutron star (for example, moment of inertia and mass) would yield a significantly stronger constraint: It would restrict the parameter space not to one side of a surface but to the surface itself. And a subsequent observation of two different parameters for a different neutron star would then restrict one to the intersection of two surfaces. We exhibit the result of simultaneous observations of mass and moment of inertia (expected within the next decade for one member of the binary pulsar J0737-3039 [13,14]) and of mass and radius. Gravitational-wave observations of binary inspiral can again measure two properties of a single star: both mass and an observable roughly described as the final frequency before plunge (the departure of the waveform from a point-particle inspiral); and related work in progress examines the accuracy with which one can extract EOS parameters from interferometric observations of gravitational waves in the inspiral and merger of a binary neutron-star system [11].

*Conventions*: We use cgs units, denoting rest-mass density by $\rho$, and energy density $/c^2$ by $\epsilon$. We define rest-mass density as $\rho = m_B n$ where $m_B = 1.66 \times 10^{-24}$ g and $n$ is the baryon number density. In Sec. III and Appendix A, however, we set $c = 1$ to simplify the equations and add a footnote on restoring $c$.

## II. CANDIDATES

A test of how well a parametrized EOS can approximate the true EOS of cold matter at high density is how well it approximates candidate EOSs. We consider a wide array of candidate EOSs, covering many different generation methods and potential species. Because the parametrized EOS is intended to distinguish the parts of parameter space allowed and ruled out by present and future observations, the collection includes some EOSs that no longer satisfy known observational constraints. Many of the candidate EOSs were considered in Refs. [5,12,14]; and we call them by the names used in those papers.

For plain $npe\mu$ nuclear matter, we include:

(i) two potential-method EOSs (PAL6 [15] and SLy [16]);
(ii) eight variational-method EOSs (APR1-4 [17], FPS [18], and WFF1-3 [19]);
(iii) one nonrelativistic (BBB2 [20]) and three relativistic (BPAL12 [21], ENG [1] and MPA1 [22]) Brueckner-Hartree-Fock EOSs; and
(iv) three relativistic mean-field theory EOSs (MS1-2 and one we call MS1b, which is identical to MS1 except with a low symmetry energy of 25 MeV [23]).

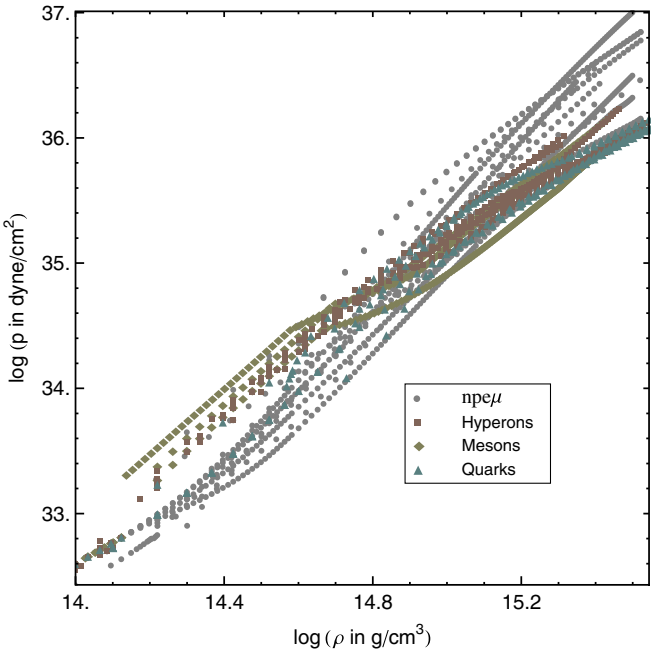


FIG. 1 (color online). Pressure versus rest mass density for the set of candidate EOS tables considered in the parametrization.

We also consider models with hyperons, pion and kaon condensates, and quarks, and will collectively refer to these EOSs as $K/\pi/H/q$ models:

(i) one neutron-only EOS with pion condensates (PS [24]);
(ii) two relativistic mean-field theory EOSs with kaons (GS1-2 [25]);
(iii) one effective-potential EOS including hyperons (BGN1H1 [26]); eight relativistic mean-field theory EOSs with hyperons (GNH3 [27], and seven variants H1-7 [12]; one relativistic mean-field theory EOS with hyperons and quarks (PCL2 [28]); and
(iv) four hybrid EOSs with mixed APR nuclear matter and color-flavor-locked quark matter (ALF1-4 with transition density $\rho_c$ and interaction parameter $c$ given by $\rho_c = 2n_0$, $c = 0$; $\rho_c = 3n_0$, $c = 0.3$; $\rho_c = 3n_0$, $c = 0.3$; and $\rho_c = 4.5n_0$, $c = 0.3$, respectively [29]).

The tables are plotted in Fig. 1 to give an idea of the range of EOSs considered for this parametrization.

## III. PIECEWISE POLYTROPE

A polytropic EOS has the form,

$$p(\rho) = K\rho^{\Gamma}, \tag{1}$$

with $\rho$ the rest-mass density and $\Gamma$ the adiabatic index, and with energy density $\epsilon$ fixed by the first law of thermodynamics,[1] $d\frac{\epsilon}{\rho} = -pd\frac{1}{\rho}$. For $p$ of the form (1), the first law has the immediate integral

$$\frac{\epsilon}{\rho} = (1 + a) + \frac{1}{\Gamma - 1}K\rho^{\Gamma-1}, \tag{2}$$

where $a$ is a constant; and the requirement $\lim_{\rho\to 0}\epsilon/\rho = 1$ implies $a = 0$ and the standard relation $\epsilon = \rho + \frac{1}{\Gamma-1}p$.

The parametrized EOSs we consider are piecewise polytropes above a density $\rho_0$, satisfying Eqs. (1) and (2) on a sequence of density intervals, each with its own $K_i$ and $\Gamma_i$: An EOS is piecewise polytropic for $\rho \geq \rho_0$ if, for a set of dividing densities $\rho_0 < \rho_1 < \rho_2 < \cdots$, the pressure and energy density are everywhere continuous and satisfy

$$p(\rho) = K_i\rho^{\Gamma_i}, \qquad d\frac{\epsilon}{\rho} = -pd\frac{1}{\rho}, \qquad \rho_{i-1} \leq \rho \leq \rho_i. \tag{3}$$

Then, for $\Gamma \neq 1$,

$$\epsilon(\rho) = (1 + a_i)\rho + \frac{K_i}{\Gamma_i - 1}\rho^{\Gamma_i}, \tag{4}$$

with $a_i = \frac{\epsilon(\rho_{i-1})}{\rho_{i-1}} - 1 - \frac{K_i}{\Gamma_i-1}\rho_{i-1}^{\Gamma_i-1}$.

The specific enthalpy[2] $h := (\epsilon + p)/\rho$, sound velocity $v_s = \sqrt{dp/d\epsilon}$, and internal energy $e := \epsilon/\rho - 1$, are given in each density interval by

$$\begin{aligned} h(\rho) &= 1 + a_i + \frac{\Gamma_i}{\Gamma_i - 1}K_i\rho^{\Gamma_i-1}, \\ v_s(\rho) &= \sqrt{\frac{\Gamma_i p}{\epsilon + p}}, \\ e(\rho) &= a_i + \frac{K_i}{\Gamma_i - 1}\rho^{\Gamma_i-1}. \end{aligned} \tag{5}$$

Each piece of a piecewise-polytropic EOS is specified by three parameters: the initial density, the coefficient $K_i$, and the adiabatic index $\Gamma_i$. However, when the EOS at lower density has already been specified up to the chosen $\rho_i$, continuity of pressure restricts $K_{i+1}$ to the value

$$K_{i+1} = \frac{p(\rho_i)}{\rho_i^{\Gamma_{i+1}}}. \tag{6}$$

Thus each additional region requires only two additional parameters, $\rho_i$ and $\Gamma_{i+1}$. Furthermore, if the initial density of an interval is chosen to be a fixed value for the parame-

[1] In this section, for simplicity of notation, $c = 1$. To rewrite the equations in cgs units, replace $p$ and $K$ in each occurrence by $p/c^2$ and $K/c^2$. Both $\epsilon$ and $\rho$ have units g/cm$^3$.

[2] A note on terminology: When the entropy vanishes, the specific enthalpy, $h = (\epsilon + p)/\rho$, and Gibbs free energy, $g = (\epsilon + p)/\rho - Ts$, coincide. For nonzero entropy, it is the term $gdM_0 = \mu dN$ that appears in the first law of thermodynamics, where $\mu = gm_B$ is the chemical potential.

trization, specifying the EOS on the density interval requires only a single additional parameter.

## IV. FITTING THE CANDIDATES

To fit the true neutron-star EOS, we must ensure that a wide variety of candidate EOSs are well fit by some set of parameter values of our parametrized EOS. In this section we describe the fit we use and the results of that fit.

There is general agreement on the low-density EOS for cold matter, and we adopt the version (SLy) given by Douchin and Haensel [16]. Substituting an alternative low-density EOS from, for example, Negele and Vautherin [30], alters by only a few percent the observables we consider in examining astrophysical constraints, both because of the rough agreement among the candidate EOSs and because the low-density crust contributes little to the mass, moment of inertia, or radius of the star.

Each choice of a piecewise-polytropic EOS above nuclear density is matched to this low-density EOS as follows: The lowest-density piece of the piecewise-polytropic $p(\rho)$ curve is extended to lower densities until it intersects the low-density EOS, and the low-density EOS is used at densities below the intersection point. This matching method yields a monotically increasing $p = p(\rho)$ without introducing additional parameters. It omits EOSs with values of $p_1$ and $\Gamma_1$ that are incompatible, i.e., for which the slope of the $\log p$ vs $\log\rho$ curve is too shallow to reach the pressure $p_1$ from the low-density part of the EOS. However it still accommodates a much larger region of parameter space than that spanned by the candidate EOSs. (The precise choice of matching algorithm has little influence on the final fit for the reasons given in the previous paragraph.)

The accuracy with which a piecewise polytrope $\{\rho_i, K_i, \Gamma_i\}$, approximates a candidate EOS is measured by the rms residual of the fit to $m$ tabulated points $\rho_j$, $p_j$:

$$\sqrt{\frac{1}{m}\left(\sum_i \sum_{\substack{j \\ \rho_i < \rho_j \leq \rho_{i+1}}} (\log p_j - \log K_i + \Gamma_i \log \rho_j)^2\right)}. \qquad (7)$$

In each case, we compute the residual only up to $\rho_{\max}$, the central density of the maximum-mass nonrotating model based on the candidate EOS. Because astrophysical observations can depend on the high-density EOS only up to the value of $\rho_{\max}$ for that EOS, only the accuracy of the fit below $\rho_{\max}$ is relevant.

The accuracy of a choice of parameter space is measured by the average residual of its fits to each EOS in the collection. For each EOS, we use a Levenberg-Marquardt algorithm to minimize the residual (7) over the parameter space. Even with a robust algorithm, the nonlinear fitting with varying dividing densities is sensitive to initial conditions. Multiple initial parameters for free fits are constructed using fixed-region fits of several possible dividing densities, and the global minimum of the resulting residuals is taken to indicate the best fit for the candidate EOS.

We begin with a single polytropic region in the core, specified by two parameters: the index $\Gamma_1$ and a pressure $p_1$ at some fixed density. Here, with a single polytrope, the choice of that density is arbitrary; for more than one polytropic piece, we will for convenience take that density to be the dividing density $\rho_1$ between the first two polytropic regions. Changing the value of $p_1$ moves the polytropic $p(\rho)$ curve up or down, keeping the logarithmic slope $\Gamma_1 = d\log p/d\log\rho$ fixed. The low-density SLy EOS is fixed, and the density $\rho_0$ where the polytropic EOS intersects SLy changes as $p_1$ changes. The polytropic index $K_1$ is determined by Eq. (6). This is referred to as a one free piece fit. We then consider two-piece and three-piece fits: two polytropic regions within the core, specified by the four parameters $\{p_1, \Gamma_1, \rho_1, \Gamma_2\}$, as well as three polytropic regions specified by the six parameters $\{p_1, \Gamma_1, \rho_1, \Gamma_2, \rho_3, \Gamma_3\}$, where, in each case, $p_1 \equiv p(\rho_1)$. Again changing $p_1$ translates the piecewise-polytropic EOS of the core up or down, keeping its shape fixed.

The accuracy of each parametrization (one, two, or three pieces), measured by the rms residual of Eq. (7), is portrayed in Table I. The table lists the average and maximum rms residuals over the set of 34 candidate EOSs. (The ''fixed'' fit is described below.)

For nucleon EOSs, the four-parameter fit of two free polytropic pieces models the behavior of candidates well; but this kind of four-parameter EOS does not accurately fit EOSs with hyperons, kaon or pion condensates, and/or quark matter. Many require three polytropic pieces to capture the stiffening around nuclear density, a subsequent softer phase transition, and then final stiffening. On the other hand, the six parameters required to specify three free polytropic pieces exceeds the bounds of what may be reasonably constrained by the small set of model-independent astrophysical measurements. An alternative four-parameter fit can be made to all EOSs if the transition densities are held fixed for all candidate EOSs (see below).

The hybrid quark EOS ALF3, which incorporates a QCD correction parameter for quark interactions, exhibits the worst fit to a one-piece polytropic EOS with residual 0.111, to the three-piece fixed-region EOS with residual 0.042, and to the three-piece varying region EOS with residual 0.042. It has a residual from the two-piece fit of 0.044, somewhat less than the worst fit EOS, BGN1H1, an effective-potential EOS that includes all possible hyperons and has a two-piece fit residual of 0.056.

A good fit is found for three polytropic pieces with fixed divisions: between the first and second pieces at $\rho_1 = 10^{14.7}$ g/cm$^3$ $= 1.85\rho_{\text{nuc}}$ and a division between the second and third pieces fixed at $\rho_2 = 10^{15.0}$ g/cm$^3$. The EOS is specified by choosing the adiabatic indices $\{\Gamma_1, \Gamma_2, \Gamma_3\}$ in each region, and the pressure $p_1$ at the first dividing density, $p_1 = p(\rho_1)$. A diagram of this parametrization is

TABLE I. Average residuals resulting from fitting the set of candidate EOSs with various types of piecewise polytropes. Free fits allow dividing densities between pieces to vary. The fixed three-piece fit uses $10^{14.7}$ g/cm$^3$ or roughly $1.85\rho_{\rm nuc}$ and $10^{15.0}$ g/cm$^3$ or $3.70\rho_{\rm nuc}$ for all EOSs. Tabled are the rms residuals of the best fits averaged over the set of candidates. The set of 34 candidates includes 17 candidates containing only $npe\mu$ matter and 17 candidates with hyperons, pion or kaon condensates, and/or quark matter. Fits are made to tabled points in the high-density region between $10^{14.3}$ g/cm$^3$ or $0.74\rho_{\rm nuc}$ and the central density of a maximum-mass spherical star calculated using that table.

| Type of fit | All | $npe\mu$ | $K/\pi/h/q$ |
|---|---|---|---|
| Mean rms residual | | | |
| One free piece | 0.0386 | 0.0285 | 0.0494 |
| Two free pieces | 0.0147 | 0.0086 | 0.0210 |
| Three fixed pieces | 0.0127 | 0.0098 | 0.0157 |
| Three free pieces | 0.0071 | 0.0056 | 0.0086 |
| Standard deviation of rms residual | | | |
| One free piece | 0.0213 | 0.0161 | 0.0209 |
| Two free pieces | 0.0150 | 0.0060 | 0.0188 |
| Three fixed pieces | 0.0106 | 0.0063 | 0.0130 |
| Three free pieces | 0.0081 | 0.0039 | 0.0107 |

shown in Fig. 2. For this four-parameter EOS, best-fit parameters for each candidate EOS give a residual of 0.043 or better, with the average residual over 34 candidate EOSs of 0.013. Note that the density of departure from the fixed low-density EOS is still a fitted parameter for this scheme.

The dividing densities for our parametrized EOS were chosen by minimizing the rms residuals over the set of 34 candidate EOSs. For two dividing densities, this is a two-dimensional minimization problem, which was solved by alternating between minimizing average rms residual for upper or lower density while holding the other density fixed. The location of the best dividing points is fairly robust over the subclasses of EOSs, as illustrated in Fig. 3.

With the dividing points fixed, taking the pressure $p_1$ to be the pressure at $\rho_1 = 1.85\rho_{\rm nuc}$, is indicated by the empirical work of Lattimer and Prakash [5] that finds a strong correlation between pressure at fixed density (near this value) and the radius of $1.4M_\odot$ neutron stars. This choice

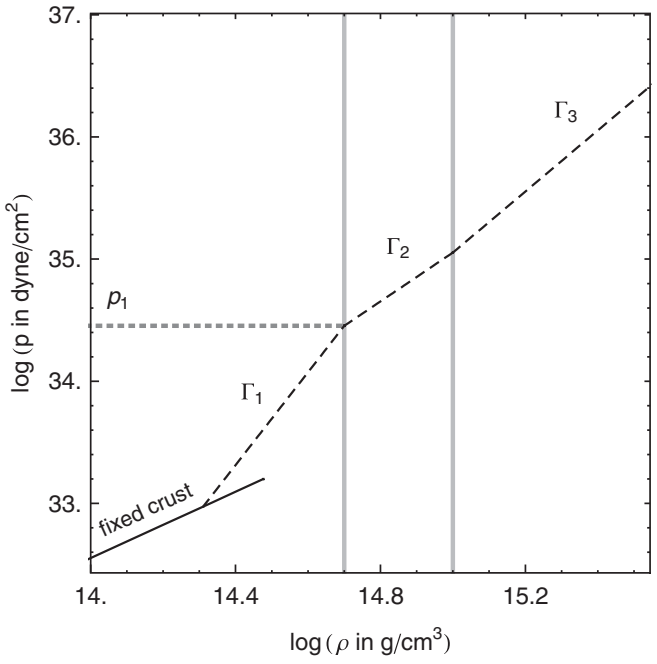


FIG. 2. The fixed-region fit is parametrized by adiabatic indices $\{\Gamma_1, \Gamma_2, \Gamma_3\}$ and by the pressure $p_1$ at the first dividing density.

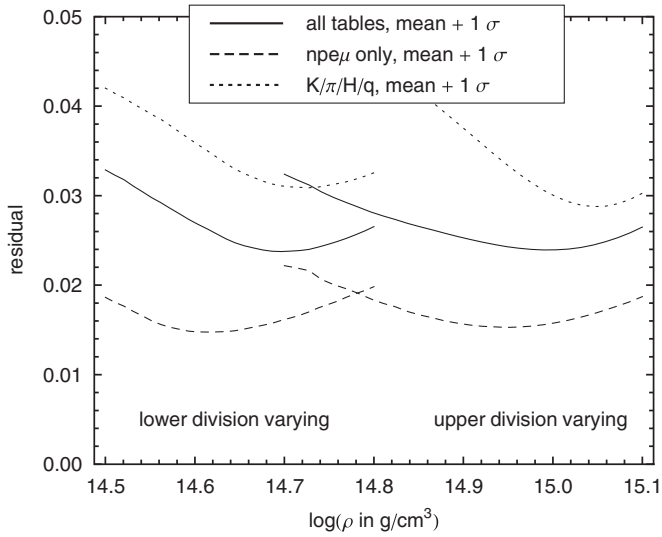


FIG. 3. Subsets of EOSs with and without kaons, hyperons, meson condensates, or quarks, show a fairly robust choice of dividing densities whose fit to the candidate EOSs minimizes residual error. The mean plus 1 standard deviation of residuals for each subset of candidate EOSs is plotted against the choice of lower and upper dividing densities $\rho_1$ and $\rho_2$. The left curves show mean residual versus $\rho_1$ with $\rho_2$ fixed at $10^{15.0}$ g/cm$^3$. The right three curves show mean residual versus $\rho_2$, with $\rho_1$ fixed at $10^{14.7}$ g/cm$^3$.

of parameter allows us to examine (in Sec. V E) the relation between $p_1$ and the radius; and we expect a similar correlation between $p_1$ and the frequency at which neutron-star inspiral dramatically departs from point-particle inspiral for neutron stars near this mass.

Since there are not many astrophysical constraints on the EOS, it is desirable to use one of the four-parameter fits (two free pieces or three fixed). Observations of pulsars that are not accreting indicate masses below $1.45M_\odot$ (see Sec. V), and the central density of these stars is below $\rho_2$ for almost all EOSs. Then only the three parameters $\{p_1, \Gamma_1, \Gamma_2\}$ of the fixed piece parametrization are required to specify the EOS for moderate mass neutron stars. This class of observations can then be treated as a set of constraints on a 3-dimensional parameter space. Similarly, because maximum-mass neutron stars ordinarily have most matter in regions with densities greater than the first dividing density, their structure is insensitive to the first adiabatic index. The three-piece parametrization does a significantly better job above $\rho_2$ because phase transitions above that density require a third polytropic index $\Gamma_3$. If the remaining three parameters can be determined by pulsar observations, then observations of more massive, accreting stars can constrain $\Gamma_3$.

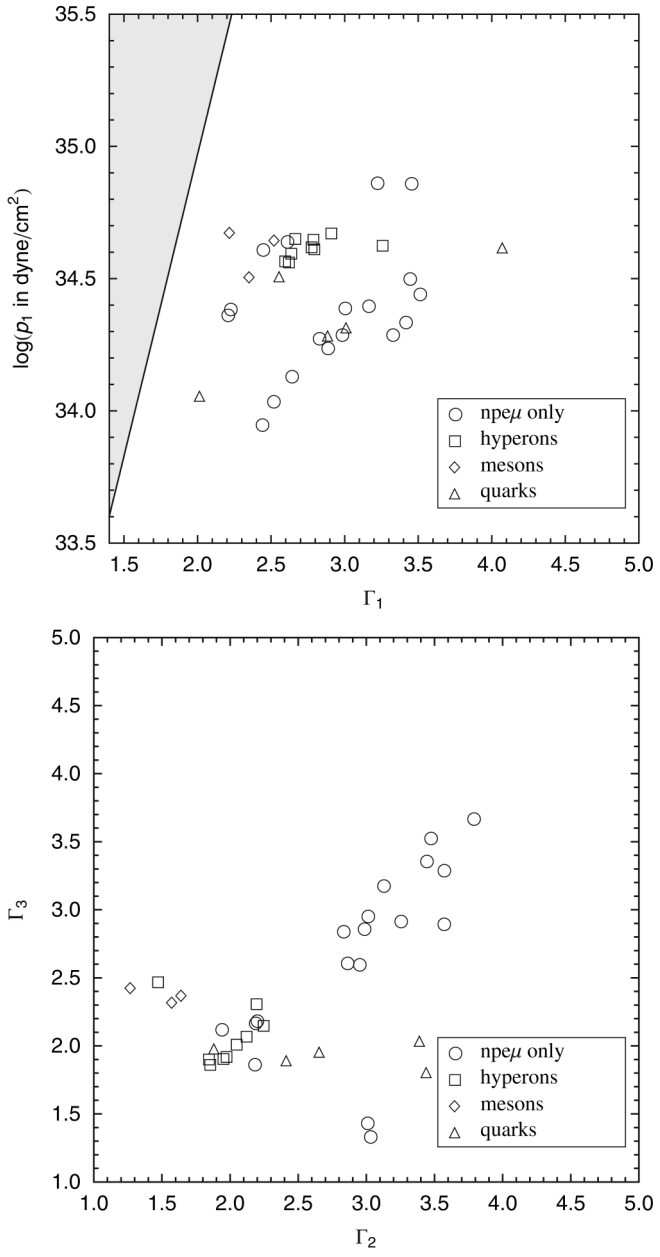


FIG. 4. Parametrized EOS fits to the set of 34 candidate EOS tables. There are 17 EOSs with only ordinary nuclear matter ($n$, $p$, $e$, $\mu$); 9 have only hyperons in addition to ordinary matter; 3 include meson condensates plus ordinary matter; 5 include quarks plus other matter (PCL2 also has hyperons). $\Gamma_2 < 3.5$ and $\Gamma_3 < 2.5$ for all EOSs with hyperons, meson condensates, and/or quark cores. The shaded region corresponds to incompatible values of $p_1$ and $\Gamma_1$, as discussed in the text.

The best-fit parameter values of the candidate EOSs are shown in Fig. 4 and listed in Table III of Appendix C. The worst fits of the fixed-region fit are the hybrid quark EOSs ALF1 and ALF2, and the hyperon-incorporating EOS BGN1H1. For BGN1H1, the relatively large residual is due to the fact that the best-fit dividing densities of BGN1H1 differ strongly from the average best dividing densities. Although BGN1H1 is well fit by three pieces with floating densities, the reduction to a four-parameter fit limits the resolution of EOSs with such structure. The hybrid quark EOSs, however, have more complex structure that is difficult to resolve accurately with a small number of polytropic pieces. Still, the best-fit polytrope EOS is able to reproduce the neutron-star properties predicted by the hybrid quark EOS.

In Appendix C, Table III compares neutron-star properties for each EOS to their values for the best-fit piecewise polytrope. The mean error and standard deviation for each characteristic is also listed.

## V. ASTROPHYSICAL CONSTRAINTS ON THE PARAMETER SPACE

Adopting a parametrized EOS allows one to phrase each observational constraint as a restriction to a subset of the parameter space. In Subsecs. V A, V B, V C, and V D, we find the constraints imposed by causality, by the maximum observed neutron-star mass and the maximum observed neutron-star spin, and by a possible observation of gravitational redshift. We then examine, in Subsec. V E, constraints from the simultaneous measurement of mass and moment of inertia and of mass and radius. We exhibit in Subsec. V F the combined constraint imposed by causality, maximum observed mass, and a future moment of inertia measurement of a star with known mass.

In exhibiting the constraints, we show a region of the 4-dimensional parameter space large enough to encompass the 34 candidate EOSs considered above.

The graphs in Fig. 4 display the ranges $10^{33.5}$ dyne/cm$^2$ $< p_1 < 10^{35.5}$ dyne/cm$^2$, $1.4 < \Gamma_1 < 5.0$, $1.0 < \Gamma_2 < 5.0$, and $1.0 < \Gamma_3 < 5.0$. Also shown is the location in parameter space of the best fit to each candidate EOS. The shaded region in the top graph corresponds to incompatible values of $p_1$ and $\Gamma_1$ mentioned in Sec. IV.

To find the constraints on the parametrized EOS imposed by the maximum observed mass and spin, one finds the maximum mass and spin of stable neutron stars based on the EOS associated with each point of parameter space. A subtlety in determining these maximum values arises from a break in the sequence of stable equilibria—an island of unstable configurations—for some EOSs. The unstable island is typically associated with phase transitions in a way we now describe.

Spherical Newtonian stars described by EOSs of the form $p = p(\rho)$ are unstable when an average value $\bar{\Gamma}$ of the adiabatic index falls below $4/3$. The stronger-than-Newtonian gravity of relativistic stars means that instability sets in for larger values of $\bar{\Gamma}$, and it is ordinarily this increasing strength of gravity that sets an upper limit on neutron-star mass. EOSs with phase transitions, however, temporarily soften above the critical density and then stiffen again at higher densities. As a result, configurations whose inner core has density just above the critical density can be unstable, while configurations with greater central density can again be stable. Models with this behavior are considered, for example, by Glendenning and Kettner [31], Bejger *et al.* [8], and by Zdunik *et al.* [7] (these latter authors, in fact, use piecewise-polytropic EOSs to model phase transitions).

For our parametrized EOS, instability islands of this kind can occur for $\Gamma_2 \lesssim 2$, when $\Gamma_1 \gtrsim 2$ and $\Gamma_3 \gtrsim 2$. A slice of the 4-dimensional parameter space with constant $\Gamma_1$ and $\Gamma_3$ is displayed in Fig. 5. The shaded region corresponds to EOSs with islands of instability. Contours are also shown for which the maximum mass for each EOS has the constant value $1.7M_\odot$ (lower contour) and $2.0M_\odot$ (upper contour).

An instability point along a sequence of stellar models with constant angular momentum occurs when the mass is maximum. On a mass-radius curve, stability is lost in the direction for which the curve turns counterclockwise about the maximum mass and is regained when it turns clockwise. In the bottom graph of Fig. 5, mass-radius curves are plotted for six EOSs, labeled A–F, associated with six correspondingly labeled EOSs in the top figure. The sequences associated with EOSs B, C, and E have two maximum masses (marked by black dots in the lower figure) separated by a minimum mass. As one moves along the sequence from larger to smaller radius—from lower to higher density, stability is temporarily lost at the first maximum mass, regained at the minimum mass, and permanently lost at the second maximum mass.

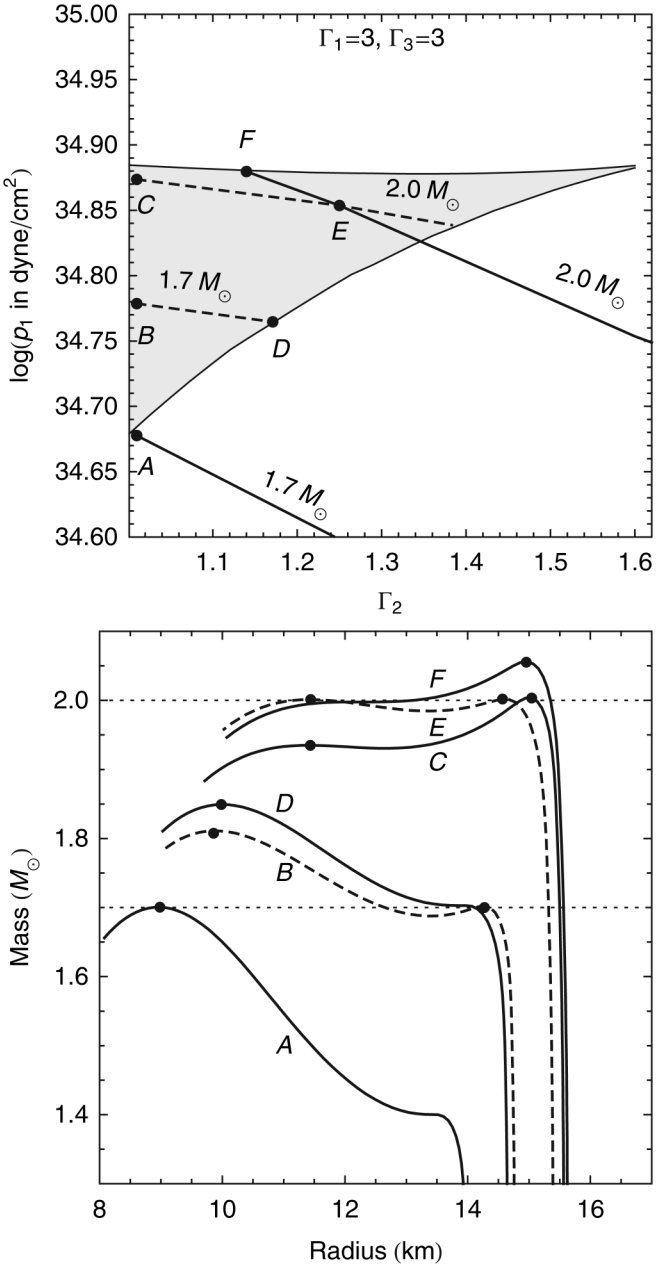


FIG. 5. The region in parameter space where two stable neutron-star sequences can occur is shaded in the top figure. Contours of constant maximum mass are also shown. The higher central density maximum-mass contour is solid while the lower central density maximum-mass contour is dashed. Mass-radius curves are plotted for several EOSs in the bottom figure. Although difficult to see, EOS C does in fact have a second stable sequence.

It is clear from each graph in Fig. 5 that either of the two local maxima of mass can be the global maximum. On the lower boundary (containing EOSs A and D), the lower-density maximum mass first appears, but the upper-density maximum remains the global maximum in a neighborhood of the boundary. Above the upper boundary (containing EOS F), the higher-density maximum has disappeared, and

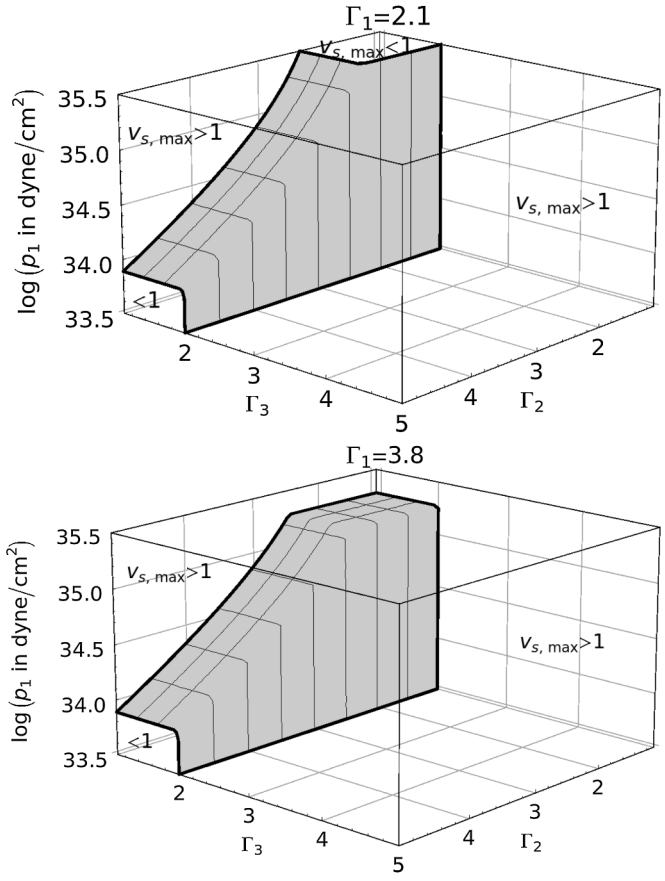


FIG. 6. Causality constraints are shown for two values of $\Gamma_1$. For each EOS in the parameter space the maximum speed of sound over all densities is used. The shaded surface separates the EOS parameter space into a region behind the surface allowed by causality (labeled $v_{s,\max} < 1$) and a region in which corresponding EOSs violate causality at any density (labeled $v_{s,\max} > 1$).

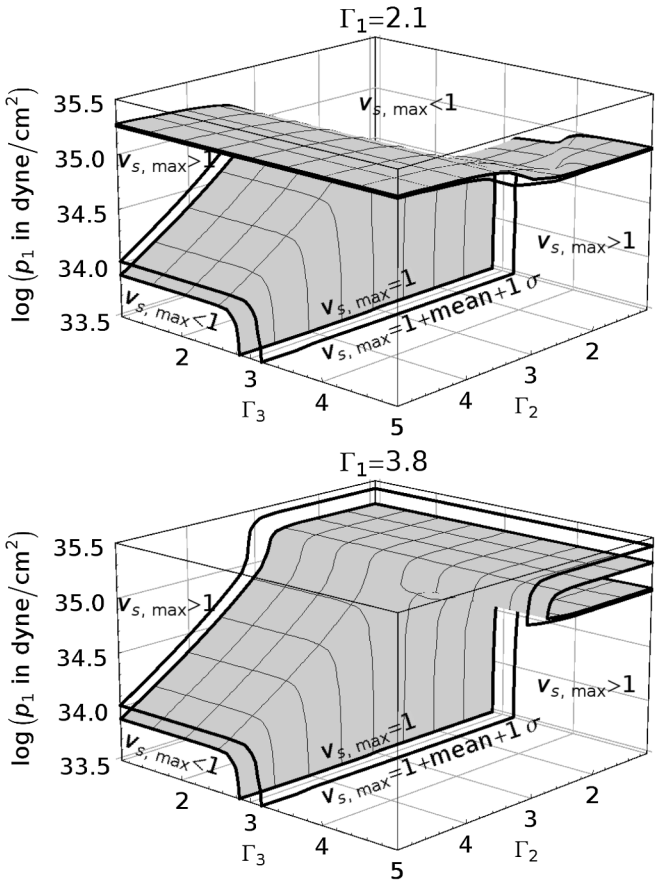


FIG. 7. Causality constraint as in Fig. 6. However, here, only the maximum speed of sound up to the central density of the maximum-mass star is considered. A second, outlined surface shows a weaker constraint to accommodate the expected error in the speed of sound associated with a piecewise-polytropic approximation to an EOS. With $\sigma$ the standard deviation in $v_{s,\max}$ between an EOS and its parametrized representation, as measured by the collection of candidate EOSs, the outlined surface depicts $v_{s,\max} = 1 + \text{mean} + 1\sigma = 1.12$ constraint.

near the upper boundary the lower-density maximum is the global maximum.

### A. Causality

For an EOS to be considered physically reasonable, the adiabatic speed of sound $v_s$ cannot exceed the speed of light. An EOS is ruled out by causality if $v_s > 1$ for any density below the central density $\rho_{\max}$ of the maximum-mass neutron star for that EOS. (If $v_s > 1$ only above $\rho_{\max}$, the EOS is astrophysically indistinguishable from one altered to have $v_s < 1$ above $\rho_{\max}$ and thus should not be ruled out.)

We exhibit the causality constraint in two ways, first by simply requiring that each piecewise polytrope be causal at all densities and then by requiring only that it be causal below $\rho_{\max}$. The first, unphysically strong, constraint, shown in Fig. 6, is useful for an intuitive understanding of the constraint: The speed of sound is a measure of the stiffness of the EOS, and requiring causality eliminates the largest values of $\Gamma_i$ and $p_1$.

Figure 7 shows the result of restricting the constraint to densities below $\rho_{\max}$, with the speed of sound given by Eq. (5). A second surface is shown to account for the inaccuracy with which a piecewise-polytropic approximation to an EOS represents the speed of sound. In all but one case (BGN1H1) the fits to the candidate EOSs overpredict the maximum speed of sound, but none of the fits to the candidate EOSs mispredict whether the candidate EOS is causal or acausal by more than 11% (fractional difference between fit and candidate). We adopt as a suitable causality constraint a restriction to a region bounded by the surface $v_{s,\max} = 1 + \text{mean} + 1\sigma = 1.12$, corresponding to the mean plus 1 standard deviation in the error between $v_{s,\max}$ for the candidate and best-fit EOSs.

In the lower parts of each graph in Fig. 7, where $p_1 < 10^{35}$ dyne/cm$^2$, the bounding surface has the character of the first causality constraint, with the restriction on each of the three variables $p_1$, $\Gamma_2$, and $\Gamma_3$ becoming more stringent

as the other parameters increase, and with $\Gamma_3$ restricted to be less than about 3. In this low-pressure part of each graph, the surface is almost completely independent of the value of $\Gamma_1$: Because the constraint takes the form $\Gamma_1 p/(\epsilon + p) \leq c^2$ (for $p \ll \epsilon$) and $p < p_1$ is so low, the constraint rules out values of $\Gamma_1$ only at or beyond the maximum $\Gamma_1$ we consider.

In the upper part of each graph, where $p_1 > 10^{35}$ dyne/cm$^2$, unexpected features arise from the fact that we impose the causality constraint only below the maximum density of stable neutron stars—below the central density of the maximum-mass star.

The most striking feature is the way the constraint surface turns over in the upper part of the top graph, where $p_1 > 10^{35}$ dyne/cm$^2$, in a way that allows arbitrarily large values of $p_1$. This occurs because, when $p_1$ is large, the density of the maximum-mass star is small, and a violation of causality typically requires high density. That is, when the density is low, the ratio $p/(\epsilon + p)$ in Eq. (5) is small. As a result, in the top graph, $v_s$ remains too small to violate causality before the maximum density is reached. In the bottom graph, with $\Gamma_1 = 3.8$, $\Gamma_1$ is now large enough in Eq. (5) that the EOS becomes acausal just below the transition to $\Gamma_2$. This is the same effect that places the upper limit on $p_1$ seen in the second graph of Fig. 6.

A second feature of the upper parts of each graph is the exact independence of the bounding surface on $\Gamma_3$. The reason is simply that in this part of the parameter space the central density of the maximum-mass star is below $\rho_2$, implying that no stable neutron stars see $\Gamma_3$.

Finally, we note that in both graphs, for small $\Gamma_2$ (the right of the graph), the EOSs yield the sequences mentioned above, in which an island of instability separates two stable sequences, each ending at a local maximum of the mass. Requiring $v_{s,\max}$ to satisfy causality for both stable regions rules out EOSs below the lower part of the bifurcated surface.

### B. Maximum mass

A stringent observational constraint on the EOS parameter space is set by the largest observed neutron-star mass. Unfortunately, the highest claimed masses are also subject to the highest uncertainties and systematic errors. The most reliable measurements come from observations of radio pulsars in binaries with neutron-star companions. The masses with tightest error bars (about $0.01M_\odot$) cluster about $1.4M_\odot$ [32]. Recent observations of millisecond pulsars in globular clusters with non-neutron-star companions have yielded higher masses: Ter 5I and Ter 5J [33], M5B [34], PSR J1903 + 0327 [35], and PSR J0437-4715 [36] all have 95% confidence limits of about $1.7M_\odot$, and the corresponding limit for NGC 6440B [37] is about $2.3M_\odot$. However these systems are more prone to systematic errors: The pulsar mass is obtained by assuming that the periastron advance of the orbit is due to general relativity. Periastron advance can also arise from rotational deformation of the companion, which is negligible for a neutron star but could be much greater for pulsars which have white dwarf or main sequence star companions. Also the mass measurement is affected by the inclination angle, which is known only for the very nearby PSR J0437-4715. And with the accumulation of observations of these eccentric binary systems (now about a dozen) it becomes more likely that the anomalously high figure for NGC 6440B is a statistical fluke. Figure 8 shows the constraint on the EOS placed by the existence of $1.7M_\odot$ neutron stars, which we regard as secure. Also shown in the figure are the surfaces associated with maximum masses of $2.0M_\odot$ and $2.3M_\odot$.

Since all of the candidate high-mass pulsars are spinning slowly enough that the rotational contribution to their structure is negligible, the constraint associated with their observed masses can be obtained by computing the maximum mass of nonrotating neutron stars. Corresponding to each point in the parameter space is a sequence of neutron stars based on the associated parametrized EOS; and a point of parameter space is ruled out if the corresponding sequence has maximum mass below the largest observed mass. We exhibit here the division of parameter space into regions allowed and forbidden by given values of the largest observed mass.

We plot contours of constant maximum mass in Fig. 8. Because EOSs below a maximum-mass contour produce stars with lower maximum masses, the parameter space below these surfaces is ruled out. The error in the maximum mass between the candidate and best-fit piecewise-polytropic EOSs is $|\text{mean}| + 1\sigma = 1.7\%$ (the magnitude of the mean error plus 1 standard deviation in the error over the 34 candidate EOSs), so the parameters that best fit the true EOS are unlikely to be below this surface.

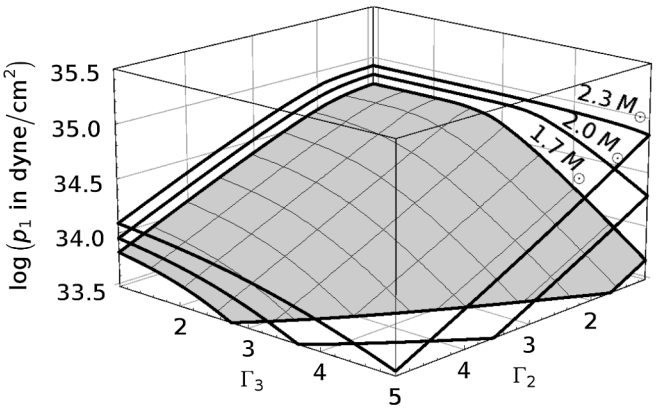


FIG. 8. The above surfaces represent the set of parameters that result in a constant maximum mass. An observation of a massive neutron star constrains the equation of state to lie above the corresponding surface. $\Gamma_1$ is set to the least constraining value at each point. The lower shaded surface represents $M_{\max} = 1.7M_\odot$; the middle and upper (outlined) surfaces represent $M_{\max} = 2.0M_\odot$ and $M_{\max} = 2.3M_\odot$, respectively.

The surfaces of Fig. 8 have minimal dependence on $\Gamma_1$, indicating that the maximum mass is determined primarily by features of the EOS above $\rho_1$. In Fig. 8 we have set $\Gamma_1$ to the least constraining value in the range we consider—to the value that gives the largest maximum mass at each point in $\{p_1, \Gamma_2, \Gamma_3\}$ space. Varying $\Gamma_1$ causes the contours to shift up, constraining the parameter space further, by a maximum of $10^{0.2}$ dyne/cm$^2$. The dependence of the contour on $\Gamma_1$ is most significant for large values of $p_1$ where the average density of a star is lower. The dependence on $\Gamma_1$ decreases significantly as $p_1$ decreases.

As discussed above, some of the EOSs produce sequences of spherical neutron stars with an island of instability separating two stable sequences, each with a local maximum of the mass. As shown in Fig. 5, this causes a contour in parameter space of constant maximum mass to split into two surfaces, one surface of parameters which has this maximum mass at the lower $\rho_c$ local maximum and another surface of parameters which has this maximum mass at higher $\rho_c$ branches. Since such EOSs allow stable models up to the largest of their local maxima, we use the least constraining surface (representing the global maximum mass) when ruling out points in parameter space.

### C. Gravitational redshift

We turn next to the constraint set by an observed redshift of spectral lines from the surface of a neutron star. We consider here only stars for which the broadening due to rotation is negligible and restrict our discussion to spherical models. The redshift is then $z = (1 - 2M/R)^{-1/2} - 1$, and measuring it is equivalent to measuring the ratio $M/R$. With no independent measurement of mass or radius, the associated constraint again restricts the parameter space to one side of a surface, to the EOSs that allow a redshift as large as the largest observed shift.[3] For spherical models, the configuration with maximum redshift for a given EOS is ordinarily the maximum-mass star. By increasing $p_1$, $\Gamma_2$, or $\Gamma_3$, one stiffens the core, increasing the maximum mass, but also increasing the radius at fixed mass. The outcome of the competition usually, but not always, yields increased redshift for larger values of these three parameters; that is, the increased maximum mass dominates the effect of increased radius at fixed mass for all but the largest values of $p_1$.

Cottam, Paerels, and Mendez [39] claim to have observed spectral lines from EXO 0748-676 with a gravitational redshift of $z = 0.35$. With three spectral lines agreeing on the redshift, the identification of the spectral features with iron lines is better founded than other claims involving only a single line. The identification remains in doubt, however, because the claimed lines have not been seen in subsequent bursts [40]. There is also a claim of a simultaneous mass-radius measurement of this system using Eddington-limited photospheric expansion x-ray bursts [41] which would rule out many EOSs. This claim is controversial, because the 95% confidence interval is too wide to rule out much of the parameter space, and we believe the potential for systematic error is understated. However, the gravitational redshift is consistent with the earlier claim of 0.35. Thus we treat $z = 0.35$ as a tentative constraint. We also exhibit the constraint that would be associated with a measurement of $z = 0.45$.

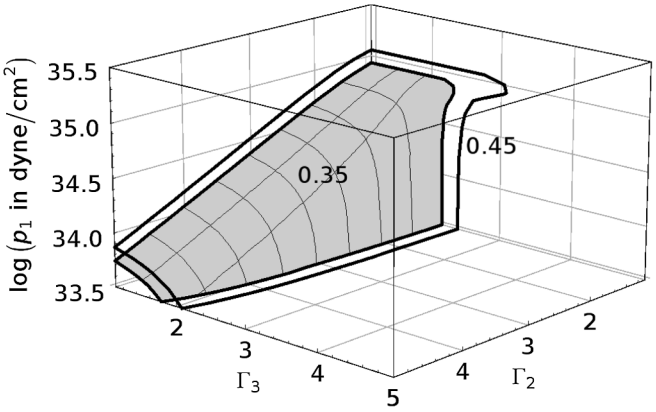


FIG. 9. Surfaces in the EOS parameter space for which the maximum redshift of stable spherical neutron stars has the values 0.35 (shaded surface) and 0.45 (outlined surface). A measured redshift from the surface of a neutron star would exclude the region of parameter space behind the corresponding surface. $\Gamma_1$ is fixed at 5.0, the least constraining in the range we considered.

Our parametrization can reproduce the maximum redshift of tabulated EOSs to 3.0% (mean + $1\sigma$). Figure 9 displays surfaces of constant redshift $z = 0.35$ and $z = 0.45$ for the least constraining value of $\Gamma_1 = 5$ in the range we consider. Surfaces with different values of $\Gamma_1$ are virtually identical for $p_1 < 10^{34.8}$ dyne/cm$^2$, but diverge for higher pressures when $\Gamma_1$ is small ($\lesssim 2.5$). In the displayed parameter space, points in front of the $z = 0.35$ surface, corresponding to stiffer EOSs in the inner core, are allowed by the potential $z = 0.35$ measurement. From the location of the $z = 0.35$ and $z = 0.45$ surfaces, it is clear that, without an upper limit on $\Gamma_1 \lesssim 2.5$, an observed redshift significantly higher than 0.35 is needed to constrain the parameter space. In particular, most of the parameter space ruled out by $z = 0.35$ is already ruled out by the $M_{\max} = 1.7M_\odot$ constraint displayed in Fig. 8.

### D. Maximum spin

Observations of rapidly rotating neutron stars can also constrain the EOS. The highest uncontroversial spin frequency is observed in pulsar Ter 5AD at 716 Hz [42]. There is a claim of 1122 Hz inferred from oscillations in

[3]One could also imagine a measured redshift small enough to rule out a class of EOSs. The minimum redshift for each EOS, however, occurs for a star whose central density is below nuclear density. Its value, $z \approx 5 \times 10^{-4}$, thus depends only on the EOS below nuclear density. (See, for example, Haensel *et al.* [38].)

x-ray bursts from XTE J1239-285 [43], but this is controversial because the statistical significance is relatively low, the signal could be contaminated by the details of the burst mechanism such as fallback of burning material, and the observation has not been repeated.

The maximum angular velocity of a uniformly rotating star occurs at the Kepler or mass-shedding limit, $\Omega_K$, with the star rotating at the speed of a satellite in circular orbit at the equator. For a given EOS, the configuration with maximum spin is the stable configuration with highest central density along the sequence of stars rotating at their Kepler limit. An EOS thus maximizes rotation if it maximizes the gravitational force at the equator of a rotating star—if it allows stars of large mass and small radius. To allow high-mass stars, the EOS must be stiff at high density, and for the radius of the high-mass configuration to be small, the EOS must be softer at low density, allowing greater compression in the outer part of the star [44,45]. In our parameter space, a high angular velocity then restricts one to a region with large values of $\Gamma_2$ and $\Gamma_3$, and small values of $p_1$ and $\Gamma_1$.

As with the maximum mass, the maximum frequency is most sensitive to the parameter $p_1$, but the frequency constraint complements the maximum-mass constraint by placing an upper limit on $p_1$ over the parameter space, rather than a lower limit.

To calculate the maximum rotation frequencies for our parametrized EOS, we used the open-source code RNS for axisymmetric rapid rotation in the updated form RNS 2.0 [46]. For a given EOS, the model with maximum spin is ordinarily close to the model with maximum mass, but that need not be true for EOSs that yield two local mass maxima. The resulting calculation of maximum rotation requires some care, and the method we use is described in Appendix B. The error incurred in using the parametrized EOS instead of a particular model is 2.7% (mean + $1\sigma$).

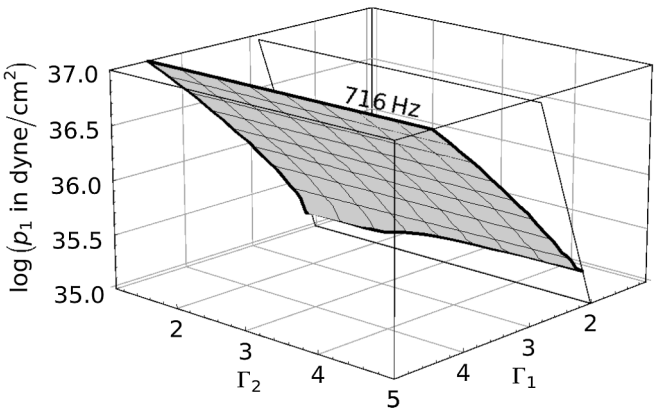


FIG. 10. The above surface represents the set of parameters that result in a maximum spin frequency of 716 Hz for the top surface. For high values of $p_1$ there is no dependence on $\Gamma_3$. The wedge at the back right is the shaded region of Fig. 4, corresponding to incompatible values of $p_1$ and $\Gamma_1$.

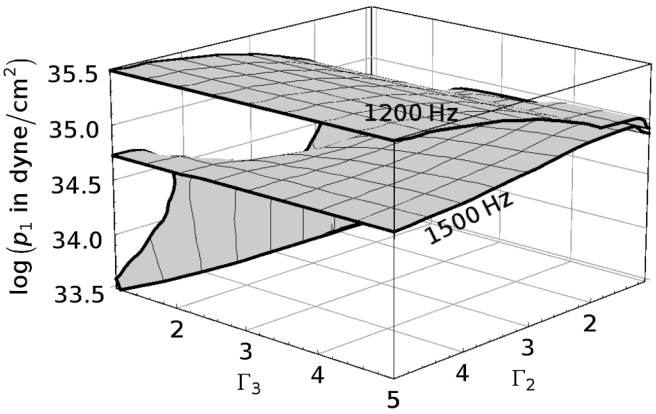


FIG. 11. The above surfaces represent the set of parameters that result in a maximum spin frequency of 1200 Hz for the top surface and 1500 Hz for the bottom surface. That is, observations of such high spin frequencies would constrain the EOS to lie below the corresponding surface. For these surfaces $\Gamma_1 = 5$, the least constraining value.

Spin frequencies of 716 Hz and even the possible 1122 Hz turn out to be very weak constraints because both are well below the Kepler frequencies of most EOSs. Thus we plot surfaces of parameters giving maximum rotation frequencies of 716 Hz in Fig. 10 and 1200 Hz and 1500 Hz in Fig. 11. The region of parameter space above the maximum observed spin surface is excluded. In the top figure, maximum-mass stars have central densities below $\rho_2$ so there is no dependence on $\Gamma_3$. In the bottom figure the least constraining value of $\Gamma_1 = 5$ is fixed. The surface corresponding to a rotation of 716 Hz only constrains the parameter space that we consider ($p_1 < 10^{35.5}$ dyne/cm$^3$) if $\Gamma_1 \lesssim 2.5$. The minimum observed rotation rate necessary to place a firm upper limit on $p_1$ is roughly 1200 Hz for $\Gamma_1 = 5$. The surface $f_{\max} = 1500$ Hz for $\Gamma_1 = 5$ is also displayed in Fig. 11 to demonstrate that much higher rotation frequencies must be observed in order to place strong limits on the parameter space.

Because it is computationally expensive to use RNS to evaluate the maximum rotation frequency for a wide range of values in a four-parameter space, one can also use an empirical formula. Haensel and Zdunik [47] found that the maximum stable rotation for a given EOS can be found from the maximum-mass spherically symmetric model for that EOS with mass $M_s$ and radius $R_s$:

$$\left(\frac{\Omega_{\max}}{10^4\ \mathrm{s}^{-1}}\right) \approx \kappa \left(\frac{M_s}{M_\odot}\right)^{1/2} \left(\frac{R_s}{10\ \mathrm{km}}\right)^{-(3/2)}. \quad (8)$$

In other words the maximum rotation is proportional to the square root of the average density of the star.

The original calculation of Haensel and Zdunik gave $\kappa = 0.77$. An overview of subsequent calculations is given by Haensel *et al.* in [48], reporting values of $\kappa = 0.76$–$0.79$ for a range of EOS sets and calculation methods

including those of [49–51]. If we calculate maximum rotations with RNS as described above, using the 34 tabulated EOSs, we find $\kappa = 0.786 \pm 0.030$. The corresponding best-fit parametrized EOSs give $\kappa = 0.779 \pm 0.027$.

### E. Moment of inertia or radius of a neutron star of known mass

The moment of inertia of the more massive component, pulsar A, in the double pulsar PSR J0737-3039 may be determined to an accuracy of 10% within the next few years [13] by measuring the advance of the system's periastron, and implications for candidate EOSs have been examined in [14,52,53]. As noted earlier, by finding both mass and moment of inertia of the same star one imposes a significantly stronger constraint on the EOS parameter space than the constraints associated with measurements of mass or spin alone: The latter restrict the EOS to the region of parameter space lying on one side of a surface, the region associated with the inequality $M_{\rm max}(p_1, \Gamma_i) > M_{\rm observed}$ or with $\Omega_{\rm max}(p_1, \Gamma_i) > \Omega_{\rm observed}$. The simultaneous measurement, on the other hand, restricts the EOS to a single surface. That is, in an $n$-dimensional parameter space, the full $n$-dimensional set of EOSs which allow a $1.338M_\odot$ model, and those EOSs for which that model has moment of inertia $I_{\rm observed}$ form the $(n-1)$-dimensional surface in parameter space given by $I(p_1, \Gamma_i, M = 1.338M_\odot) = I_{\rm observed}$. (We use here the fact that the 44 Hz spin frequency of pulsar A is slow enough that the moment of inertia is nearly that of the spherical star.) Moreover, for almost all EOSs in the parameter space, the central density of a $1.338M_\odot$ star is below the transition density $\rho_2$. Thus the surfaces of constant moment of inertia have negligible dependence on $\Gamma_3$, the adiabatic index above $\rho_2$, and the EOS is restricted to the *two-dimensional* surface in the $p_1$-$\Gamma_1$-$\Gamma_2$ space given by $I(p_1, \Gamma_1, \Gamma_2, M = 1.338M_\odot) = I_{\rm observed}$.

This difference in dimensionality means that, in principle, the simultaneous equalities that give the constraint from observing two features of the same star are dramatically stronger than the inequalities associated with measurements of mass or spin alone. In practice, however, the two-dimensional constraint surface is thickened by the error of the measurement. The additional thickness associated with the error with which the parametrized EOS can reproduce the moment of inertia of the true EOS is smaller, because the parametrized EOS reproduces the moment of inertia of the 34 candidate EOSs to within 2.9% ($|\text{mean}| + 1\sigma$).

In Fig. 12 we plot surfaces of constant moment of inertia that span the range associated with the collection of candidate EOSs. The lower shaded surface represents $I = 1.0 \times 10^{45}$ g cm$^2$. This surface has very little dependence on $\Gamma_1$ because it represents a more compact star, and thus for a fixed mass, most of the mass is in a denser state $\rho > \rho_1$. The structures of these stars do depend on $\Gamma_3$, and the corresponding dependence of $I$ on $\Gamma_3$ is shown by the separation between the two shaded surfaces in Fig. 12. The middle outlined surface represents $I = 1.5 \times 10^{45}$ g cm$^2$, and is almost a surface of constant $p_1$. The top outlined surface represents $I = 2.0 \times 10^{45}$ g cm$^2$. This surface has little dependence on $\Gamma_2$, because a star with an EOS on this surface would be less compact and thus most of its mass would be in a lower-density state $\rho < \rho_1$.

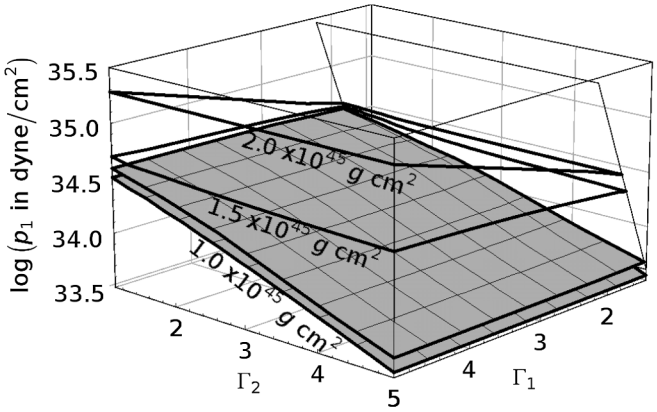


FIG. 12. The above surfaces represent the set of parameters that result in a star with a mass of $1.338M_\odot$ and a fixed moment of inertia, i.e., possible near-future measurements of PSR J0737-3039A. $I = 1.0 \times 10^{45}$ g cm$^2$ for the shaded surfaces, whose separation corresponds to varying $\Gamma_3$. $I = 1.5 \times 10^{45}$ g cm$^2$ for the middle outlined surface. $I = 2.0 \times 10^{45}$ g cm$^2$ for the top outlined surface. The wedge at the back right is the shaded region of Fig. 4, corresponding to incompatible values of $p_1$ and $\Gamma_1$.

If the mass of a neutron star is already known, a measurement of the radius constrains the EOS to a surface of constant mass and radius, $R(p_1, \Gamma_i) = R_{\rm observed}$, $M(p_1, \Gamma_i) = M_{\rm observed}$ in the 4-dimensional parameter space. The thickness of the surface is dominated by the

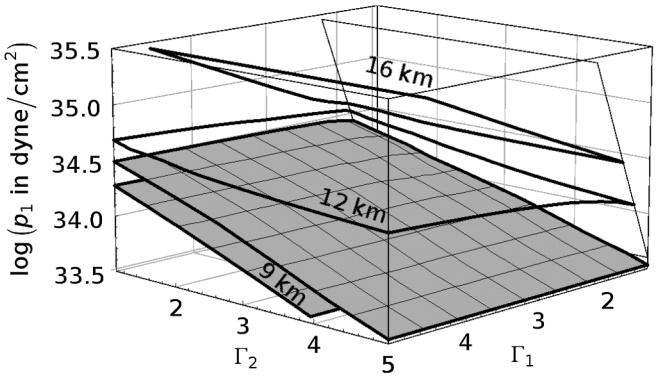


FIG. 13. The above surfaces represent the set of parameters that result in a star with a mass of $1.4M_\odot$ and a fixed radius. $R = 9$ km for the shaded surfaces, whose separation corresponds to varying $\Gamma_3$. $R = 12$ km for the middle outlined surface. $R = 16$ km for the top outlined surface. The wedge at the back right is the shaded region of Fig. 4, corresponding to incompatible values of $p_1$ and $\Gamma_1$.

uncertainty in the radius and mass measurements, since our parametrization produces the same radius as the candidate EOSs to within 1.5% ($|\text{mean}| + 1\sigma$). We plot in Fig. 13 surfaces of constant radius for a $1.4M_\odot$ star that span the range of radii associated with the collection of candidate EOSs. As with the moment of inertia, the radius depends negligibly on $\Gamma_3$ as long as the radius is greater than 11 km. For smaller radii, the variation with $\Gamma_3$ is shown by the separation between the surfaces in Fig. 13.

Very recently analyses of time-resolved spectroscopic data during thermonuclear bursts from two neutron stars in low-mass x-ray binaries were combined with distance estimates to yield $M = 1.4M_\odot$ and $R = 11$ km or $M = 1.7M_\odot$ and $R = 9$ km for EXO 1745-248 [54] and $M = 1.8M_\odot$ and $R = 10$ km for 4U 1608-52 [55], both with error bars of about 1 km in $R$. These results are more model dependent than the eventual measurement of the moment of inertia of PSR J0737-6069A, but the accuracy of the measurement of $I$ remains to be seen.

### F. Combining constraints

The simultaneous constraints imposed by causality, a maximum observed mass of $1.7M_\odot$, and a future measurement of the moment of inertia of PSR J0737-3039A, restrict the parameter space to the intersection of the allowed regions of Figs. 7, 8, and 12. We show in Fig. 14 the projection of this jointly constrained region on the $p_1$-$\Gamma_2$-$\Gamma_3$ subspace. This allows one to see the cutoffs imposed by causality that eliminate large values of $\Gamma_2$ and $\Gamma_3$ and (in the top figure) the cutoffs imposed by the existence of a $1.7M_\odot$ model that eliminates small values of $\Gamma_2$ and $\Gamma_3$.

We noted above that measuring the moment of inertia of a $1.338M_\odot$ star restricts the EOS at densities below $\rho_2$ to a 2-dimensional surface in the $p_1$-$\Gamma_1$-$\Gamma_2$ space. In the full 4-dimensional parameter space, the corresponding surfaces of constant $M$ and $I$ of Fig. 14 are then three dimensional and independent of $\Gamma_3$. Their projections onto the $p_1$-$\Gamma_2$-$\Gamma_3$ subspace are again three-dimensional and independent of $\Gamma_3$, their thickness due to the unseen dependence of the mass and moment of inertia on $\Gamma_1$. For small moments of inertia there is negligible dependence on $\Gamma_1$ so the allowed volume in Fig. 14 is thin. The thickness of the allowed volume increases as the moment of inertia increases because the dependence on $\Gamma_1$ also increases.

In Fig. 15 we show the more stringent joint constraints associated with the existence of neutron stars with masses larger than $1.7M_\odot$. We again show the constraints for three values of the moment of inertia that span the full range associated with the collection of candidate EOSs. For $I = 1.0 \times 10^{45}$ g cm$^2$ and a mass observation of at least $1.7M_\odot$, $\Gamma_3$ is required to lie in a small range, while $\Gamma_2$ is unconstrained. For larger observed masses, the constraint is even more stringent. If our parametrization is accurate, stars

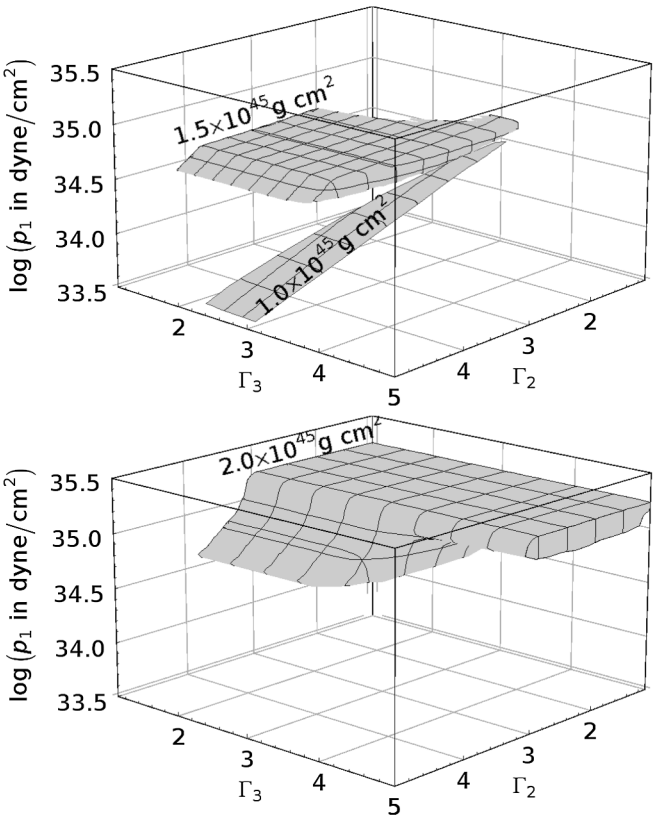


FIG. 14. The figure portrays the joint constraint imposed by causality ($v_{s,\max} < 1 + \text{mean} + 1\sigma$), the existence of a $1.7M_\odot$ neutron star, and by a future measurement of the moment of inertia $I$ of J0737-3039A. Each thick shaded surface is the volume in $\Gamma_2$-$\Gamma_3$-$p_1$ space allowed by the joint constraint for the labeled value of $I$.

with a mass greater than roughly $1.9M_\odot$ cannot exist if J0737-3039A has a moment of inertia of $I = 1.0 \times 10^{45}$ g cm$^2$ unless our parameter space is widened to include larger values of $\Gamma_2$.

For a moderate moment of inertia, $I = 1.5 \times 10^{45}$ g cm$^2$, $\Gamma_3$ is less constrained but $\Gamma_2$ is more constrained. If higher mass stars are confirmed, then the allowed region in parameter space is significantly constrained. In particular, a $2.3M_\odot$ star would roughly require that $3 < \Gamma_2 < 4$ and $\Gamma_3 < 3$.

A large moment of inertia, $I = 2.0 \times 10^{45}$ g cm$^2$, is constrained by the causality constraint. However, the maximum-mass constraint cannot rule out small values of $\Gamma_2$ and $\Gamma_3$ unless masses greater than $2.3M_\odot$ are observed.

The allowed range for $p_1$ as a function of the moment of inertia of J0737-3039A is shown in Fig. 16. The entire shaded range is allowed for a $1.7M_\odot$ maximum mass. The medium and darker shades are allowed for a $2.0M_\odot$ maximum mass. Only the range with the darker shade is allowed if a $2.3M_\odot$ star is confirmed. It should be noted that for small moments of inertia, this plot overstates the uncer-

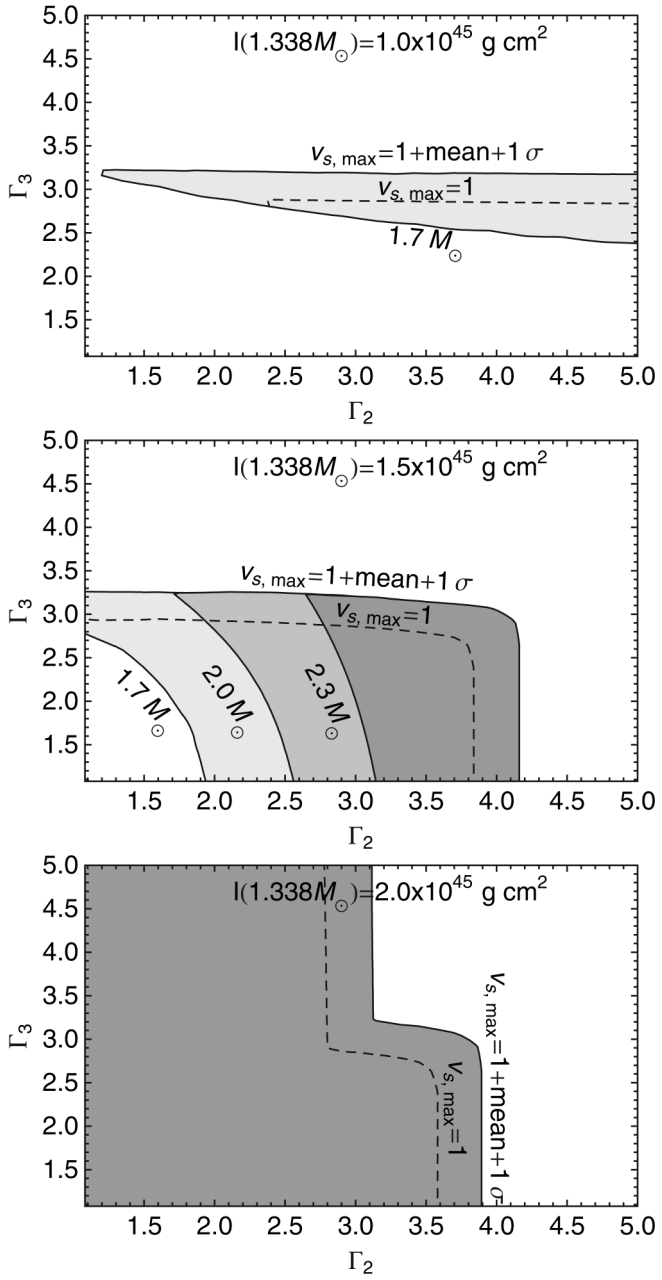


FIG. 15. The allowed values of $\Gamma_2$ and $\Gamma_3$ depend strongly on the moment of inertia of PSR J0737-3039A. In the top, middle, and bottom figures, respectively, $I$ has the values $1.0 \times 10^{45}$ g cm$^2$, $I = 1.5 \times 10^{45}$ g cm$^2$, and $I = 2.0 \times 10^{45}$ g cm$^2$. In each figure the upper curves are the $v_{s,\max} = 1$ (dotted line) and $v_{s,\max} = 1 + \text{mean} + 1\sigma = 1.12$ (solid line) causality constraints. Shading indicates a range of possible maximum-mass constraints, with increasing maximum mass leading to a smaller allowed area. All shaded areas are allowed for a $1.7M_\odot$ maximum neutron-star mass. The medium and dark shades are allowed if a $2.0M_\odot$ star is confirmed. Only the darkest shade is allowed if a $2.3M_\odot$ star is confirmed.

tainty in the allowed parameter range. As shown in Fig. 14, the allowed volume in $\Gamma_2$-$\Gamma_3$-$p_1$ space for a small moment of inertia observation is essentially 2 dimensional. If the

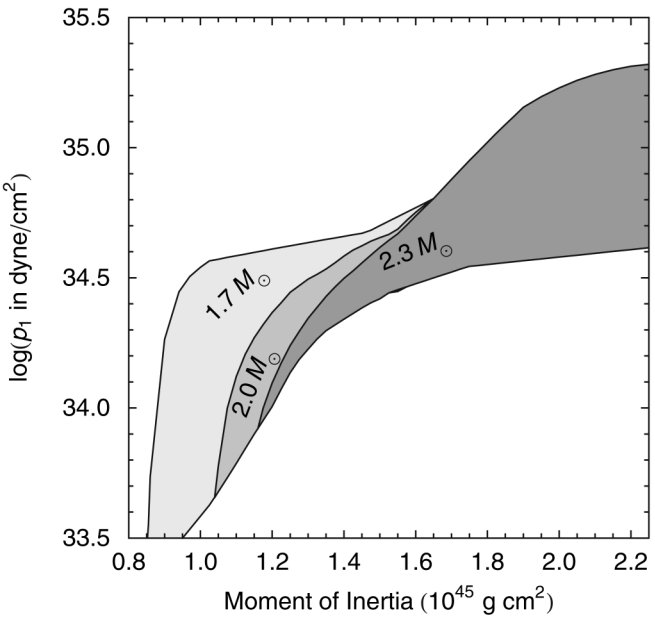


FIG. 16. The allowed range of $p_1$ as a function of the moment of inertia of J0737-3039A when combined with causality ($v_{s,\max} = 1 + \text{mean} + 1\sigma$) and observed mass constraints. All shaded areas are allowed by a $1.7M_\odot$ maximum mass. The medium and dark shades are allowed if a $2.0M_\odot$ star is confirmed. Only the darkest shade is allowed if a $2.3M_\odot$ star is confirmed.

moment of inertia is measured to be this small, then the EOS would be better parametrized with the linear combination $\alpha \log(p_1) + \beta\Gamma_2$ instead of two separate parameters $\log(p_1)$ and $\Gamma_2$.

## VI. DISCUSSION

We have shown how one can use a parametrized piecewise-polytropic EOS to systematize the study of observational constraints on the EOS of cold, high-density matter. We think that our choice of a four-parameter EOS strikes an appropriate balance between the accuracy of approximation that a larger number of parameters would provide and the number of observational parameters that have been measured or are likely to be measured in the next several years. The simple choice of a piecewise polytrope, with discontinuities in the polytropic index, leads to suitable accuracy in approximating global features of a star. But the discontinuity reduces the expected accuracy with which the parametrized EOS can approximate the local speed of sound. One can largely overcome the problem by using a minor modification of the parametrized EOS in which a fixed smoothing function near each dividing density is used to join the two polytropes.

We see that high-mass neutron stars are likely to provide the strongest constraints from a single measurement. The work dramatizes the significantly more stringent constraints associated with measurements like this, if two (or

more) physical features of the same star can be measured, and an $n$-dimensional parameter space is reduced by one (or more) dimension(s), to within the error of measurement.

The effect of EOS-dependent tidal deformation can modify the gravitational waves produced by inspiraling neutron stars. This modification is largely dependent on the radius of the neutron star. Flanagan and Hinderer [56] investigate constraints on an EOS-dependent tidal parameter, the Love number, from observations of early inspiral. A companion to this paper [11] uses the parametrized EOS in numerical simulations to examine the future constraint associated with expected gravitational-wave observations of late inspiral in binary neutron stars.

Finally, we note that the constraints from observations of different neutron-star populations constrain different density regions of the EOS. For moderate mass stars such as those found in binary pulsar systems, the EOS above $\rho_2 = 10^{15.0}$ g/cm$^3$ is unimportant. For near-maximum-mass stars, the EOS below $\rho_1 = 10^{14.7}$ g/cm$^3$ has little effect on neutron-star properties. This general behavior is independent of the details of our parametrization.

## ACKNOWLEDGMENTS

We thank P. Haensel for helpful suggestions at the start of this work and F. Özel for comments that led to corrections in one of our tables. J. Lattimer and M. Alford generously provided EOS tables from [5,29]. Other tables are from the LORENE C++ library (http://www.lorene.obspm.fr). The work was supported in part by NSF Grants No. PHY-0503366 and No. PHY-0555628, by NASA Grant No. ATP03-0001-0027, and by the Penn State Center for Gravitational-wave Physics under NSF cooperative agreement PHY-0114375.

## APPENDIX A: EVALUATING MASS, RADIUS, AND MOMENT OF INERTIA

The moment of inertia of a rotating star is the ratio $I = J/\Omega$, with $J$ the asymptotically defined angular momentum. In finding the moment of inertia of spherical models, we use Hartle's slow-rotation equations [57], adapted to piecewise polytropes. The metric of a slowly rotating star has to order $\Omega$ the form

$$ds^2 = -e^{2\Phi(r)}dt^2 + e^{2\lambda(r)}dr^2 - 2\omega(r)r^2\sin^2\theta d\phi dt + r^2 d\theta^2 + r^2\sin^2\theta d\phi^2. \quad \text{(A1)}$$

Here $\Phi$ and $\lambda$ are the metric functions of the spherical star, and the frame dragging $\omega(r)$ is obtained from the $t\phi$ component of the Einstein equation in the form

$$\frac{1}{r^4}\frac{d}{dr}\left(r^4 j\frac{d\bar{\omega}}{dr}\right) + \frac{4}{r}\frac{dj}{dr}\bar{\omega} = 0, \quad \text{(A2)}$$

with $\bar{\omega} = \Omega - \omega$ and $j(r) = e^{-\Phi}(1 - \frac{2m}{r})^{1/2}$. The angular momentum is obtained from $\omega$, which has outside the star the form $\omega = 2J/r^3$.

In adapting these equations, we roughly follow Lindblom [58], replacing $r$ as a radial variable by a generalization $\eta := h - 1$ of the Newtonian enthalpy.[4] Because $\eta$ is monotonic in $r$, one can integrate outward from its central value to the surface, where $\eta = 0$. The enthalpy, unlike $\epsilon$ and $p$, is smooth at the surface for a polytropic EOS.

For the piecewise polytropes of Sec. III, the equation of state given in terms of $\eta$ is

$$\rho(\eta) = \left(\frac{\eta - a_i}{K_i(n_i + 1)}\right)^{n_i}, \quad \text{(A3)}$$

$$p(\eta) = K_i\left(\frac{\eta - a_i}{K_i(n_i + 1)}\right)^{n_i+1}, \quad \text{(A4)}$$

$$\epsilon(\eta) = \rho(\eta)\left(1 + \frac{a_i + n_i\eta}{n_i + 1}\right), \quad \text{(A5)}$$

where $n_i = 1/(\Gamma_i - 1)$ is the polytropic index.

With $\eta$ as the indendent variable, the equations governing star and field take the form

$$(\eta + 1)e^{\Phi} = \sqrt{1 - 2M/R}, \quad \text{(A6)}$$

$$\frac{dr}{d\eta} = -\frac{r(r - 2m)}{m + 4\pi r^3 p(\eta)}\frac{1}{\eta + 1}, \quad \text{(A7)}$$

$$\frac{dm}{d\eta} = 4\pi r^2\epsilon(\eta)\frac{dr}{d\eta}, \quad \text{(A8)}$$

$$\frac{d\bar{\omega}}{d\eta} = \alpha\frac{dr}{d\eta}, \quad \text{(A9)}$$

$$\frac{d\alpha}{d\eta} = \left[-\frac{4\alpha}{r} + \frac{4\pi(\epsilon + p)(r\alpha + 4\bar{\omega})}{1 - 2m/r}\right]\frac{dr}{d\eta}, \quad \text{(A10)}$$

where $\alpha := d\bar{\omega}/dr$.

The integration to find the mass, radius, and moment of inertia for a star with given central value $\eta = \eta_c$ is equiva-

[4]Lindblom, however, uses log$h$ instead of $h - 1$ as his radial variable. The variable $\eta$ is also used by Haensel and Potekhin [9].

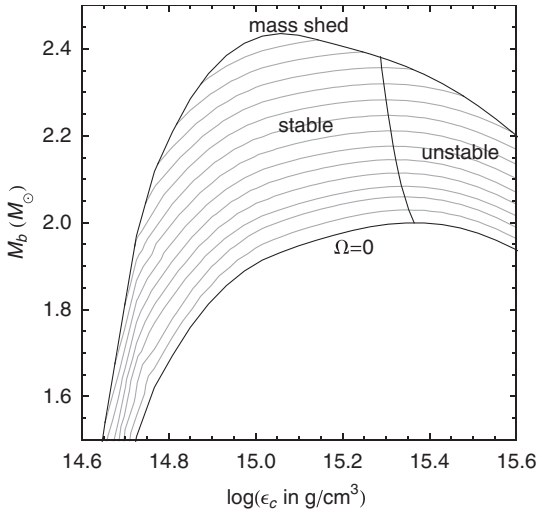


FIG. 17. The family of rotating models for a fixed EOS extends from the spherical sequence to the Kepler (mass-shed) limit $\Omega = \Omega_K$. The surface is projected into the $M_b$-$\epsilon_c$ plane and ruled by lines of constant $J$. The line of marginal stability is the roughly vertical curve through points of maximum $M_b$ on each constant $J$ line.

lent to that described in Hartle [57], with $\eta$ replacing $r$ as the independent variable.

## APPENDIX B: STABILITY OF ROTATING MODELS

For each central energy density $\epsilon_c$, the maximum angular velocity among all uniformly rotating equilibria is the Kepler or mass-shed limit $\Omega_K$. As in the spherical case, these equilibrium models may be unstable to collapse, and stability is governed by a turning-point criterion [59]: The critical points that form the line of marginal stability are extrema of mass $M$ and baryon mass $M_b$ along sequences of constant $J$; and also of $M$ and $J$ along sequences of constant $M_b$. Figure 17 shows a parametrized EOS whose maximally rotating stable star is at the intersection of the instability line and the Kepler limit.

Searches to determine the marginal stability line, as in [60], have covered the set of models with sequences of constant rest mass $M_b$, extremizing $J$ on each one, or vice versa—a computationally expensive procedure. A more efficient way uses the following fact: In the 2-dimensional space of equilibria, the gradients $\nabla J$ and $\nabla M_b$ are parallel at points of marginal stability. To see this, consider a sequence of configurations of constant $J$. The tangent to the sequence is orthogonal to $\nabla J$ at all points of the sequence; and it is orthogonal to $\nabla M_b$ at a point $P$ of marginal stability, because $P$ is a turning point, where $M_b$ is an extremum. Because the space of equilibria is 2 dimensional, $\nabla M_b$ and $\nabla J$ are parallel: $dM_b \wedge dJ = 0$. Choosing the central energy density $\epsilon_c$ and axis ratio $\mathfrak{r}$ as parameters on the surface of equilibria, we can write the condition for a point of marginal stability in the form

$$\frac{\partial M_b}{\partial \epsilon_c}\frac{\partial J}{\partial \mathfrak{r}} - \frac{\partial J}{\partial \epsilon_c}\frac{\partial M_b}{\partial \mathfrak{r}} = 0. \tag{B1}$$

The maximally rotating model for a given EOS may be determined, without finding sequences of constant $J$ and $M_b$, by considering a sequence of central energy densities $\epsilon_c$. First, increase the axis ratio $\mathfrak{r}$ until the Kepler limit is found, as in the example program MAIN.C of RNS V2.0. Second, vary $\epsilon_c$ and $\mathfrak{r}$ around this point to estimate the partial derivatives of Eq. (B1). The sign of $\partial(M_b, J)/\partial(\epsilon_c, \mathfrak{r})$ will change as the Kepler limit sequence crosses the marginal stability line.

## APPENDIX C: ANALYTIC FITS TO TABULATED EOSS

### A. Low-density equation of state

We use an analytic form of the (SLy) low-density EOS that closely matches its tabulated values. With rms residual less than 0.03, $p(\rho)$ for SLy is approximated between $\rho = 10^3$ g/cm$^3$ and $\rho = 10^{14}$ g/cm$^3$ by four polytropic pieces. The four regions correspond roughly to a nonrelativistic electron gas, a relativistic electron gas, neutron drip, and the density range from neutron drip to nuclear density. Using the notation of Sec. III, the analytic form of the SLy EOS is set by the values of $K_i$, $\Gamma_i$, and $\rho_i$ listed in Table II.

### B. Comparison table

Table III compares neutron-star properties for each EOS to their values for the best-fit piecewise polytrope. The parameters for the three-piece polytropic core EOS, the corresponding residuals, as well as the observable properties of these EOSs and the error in using the best-fit parametrized EOS instead of the tabulated EOS are listed in Table III. The parametrized EOS systematically overestimates the maximum speed of sound.

TABLE II. An analytic representation of $p(\rho)$ for the SLy EOS below nuclear density uses polytropes specified by the constants listed here. $\Gamma_i$ is dimensionless, $\rho_i$ is in g/cm$^3$, and $K_i$ is in cgs units for which the corresponding value of $p$ is in units of dyne/cm$^2$. The last dividing density is the density where the low-density EOS matches the high-density EOS and depends on the parameters $p_1$ and $\Gamma_1$ of the high-density EOS.

| $K_i$ | $\Gamma_i$ | $\rho_i$ |
|---|---|---|
| $6.801\,10 \times 10^{-9}$ | 1.584 25 | |
| $1.061\,86 \times 10^{-6}$ | 1.287 33 | $2.440\,34 \times 10^{7}$ |
| $5.326\,97 \times 10^{1}$ | 0.622 23 | $3.783\,58 \times 10^{11}$ |
| $3.998\,74 \times 10^{-8}$ | 1.356 92 | $2.627\,80 \times 10^{12}$ |

TABLE III. Comparison of candidate EOSs and their best fits. The parameters that provide the best fit to the candidate EOSs as well as the residual are given. $p_1$ is in units of dyne/cm$^2$. Values for observables calculated using the tabulated EOSs are also given. $v_{s,\max}$ is the maximum adiabatic speed of sound below the central density of the maximum-mass neutron star. $M_{\max}$ is the maximum nonrotating mass configuration in units of $M_\odot$. $z_{\max}$ is the corresponding maximum gravitational redshift. $f_{\max}$ is the maximum rotation frequency in Hz, as calculated using the rotating neutron-star code RNS. $I_{1.338}$ is the moment of inertia for a $1.338M_\odot$ star in units of $10^{45}$ g cm$^2$. $R_{1.4}$ is the radius of a $1.4M_\odot$ star in units of km. The difference in calculated values for each observable when using the tabulated EOS ($O_{\rm tab}$) versus the best-fit parametrized EOS ($O_{\rm fit}$) is calculated with $(O_{\rm fit}/O_{\rm tab} - 1)100$. The last entry gives the mean and standard deviation of the errors for each observation.

| EOS | $\log(p_1)$ | $\Gamma_1$ | $\Gamma_2$ | $\Gamma_3$ | Residual | $v_{s,\max}$ | % | $M_{\max}$ | % | $z_{\max}$ | % | $f_{\max}$ | % | $I_{1.338}$ | % | $R_{1.4}$ | % |
|---|---|---|---|---|---|---|---|---|---|---|---|---|---|---|---|---|---|
| PAL6 | 34.380 | 2.227 | 2.189 | 2.159 | 0.0011 | 0.693 | 1.37 | 1.477 | −0.47 | 0.374 | −0.51 | 1660 | −0.97 | 1.051 | −2.03 | 10.547 | −0.54 |
| SLy | 34.384 | 3.005 | 2.988 | 2.851 | 0.0020 | 0.989 | 1.41 | 2.049 | 0.02 | 0.592 | 0.81 | 1810 | 0.10 | 1.288 | −0.08 | 11.736 | −0.21 |
| APR1 | 33.943 | 2.442 | 3.256 | 2.908 | 0.019 | 0.924 | 9.94 | 1.683 | −1.60 | 0.581 | 2.79 | 2240 | 1.05 | 0.908 | −2.57 | 9.361 | −1.85 |
| APR2 | 34.126 | 2.643 | 3.014 | 2.945 | 0.0089 | 1.032 | 0.42 | 1.808 | −1.50 | 0.605 | 0.33 | 2110 | −0.02 | 1.024 | −2.34 | 10.179 | −1.57 |
| APR3 | 34.392 | 3.166 | 3.573 | 3.281 | 0.0091 | 1.134 | 2.72 | 2.390 | −1.00 | 0.704 | 0.57 | 1810 | −0.14 | 1.375 | −1.59 | 12.094 | −0.96 |
| APR4 | 34.269 | 2.830 | 3.445 | 3.348 | 0.0068 | 1.160 | 1.45 | 2.213 | −1.08 | 0.696 | 0.22 | 1940 | 0.05 | 1.243 | −1.36 | 11.428 | −0.90 |
| FPS | 34.283 | 2.985 | 2.863 | 2.600 | 0.0050 | 0.883 | 2.29 | 1.799 | −0.03 | 0.530 | 0.67 | 1880 | 0.11 | 1.137 | 0.03 | 10.850 | 0.12 |
| WFF1 | 34.031 | 2.519 | 3.791 | 3.660 | 0.018 | 1.185 | 7.86 | 2.133 | −0.29 | 0.739 | 2.21 | 2040 | 0.30 | 1.085 | 0.10 | 10.414 | 0.02 |
| WFF2 | 34.233 | 2.888 | 3.475 | 3.517 | 0.017 | 1.139 | 7.93 | 2.198 | −0.14 | 0.717 | 0.71 | 1990 | 0.03 | 1.204 | −0.59 | 11.159 | −0.28 |
| WFF3 | 34.283 | 3.329 | 2.952 | 2.589 | 0.017 | 0.835 | 8.11 | 1.844 | −0.48 | 0.530 | 2.26 | 1860 | 0.59 | 1.160 | −0.25 | 10.926 | −0.12 |
| BBB2 | 34.331 | 3.418 | 2.835 | 2.832 | 0.0055 | 0.914 | 7.75 | 1.918 | 0.10 | 0.574 | 0.97 | 1900 | 0.47 | 1.188 | 0.17 | 11.139 | −0.29 |
| BPAL12 | 34.358 | 2.209 | 2.201 | 2.176 | 0.0010 | 0.708 | 1.03 | 1.452 | −0.18 | 0.382 | −0.29 | 1700 | −1.03 | 0.974 | 0.20 | 10.024 | 0.67 |
| ENG | 34.437 | 3.514 | 3.130 | 3.168 | 0.015 | 1.000 | 10.71 | 2.240 | −0.05 | 0.654 | 0.39 | 1820 | −0.44 | 1.372 | −0.97 | 12.059 | −0.69 |
| MPA1 | 34.495 | 3.446 | 3.572 | 2.887 | 0.0081 | 0.994 | 4.91 | 2.461 | −0.16 | 0.670 | −0.05 | 1700 | −0.18 | 1.455 | −0.41 | 12.473 | −0.26 |
| MS1 | 34.858 | 3.224 | 3.033 | 1.325 | 0.019 | 0.888 | 12.44 | 2.767 | −0.54 | 0.606 | −0.52 | 1400 | 1.67 | 1.944 | −0.09 | 14.918 | 0.06 |
| MS2 | 34.605 | 2.447 | 2.184 | 1.855 | 0.0030 | 0.582 | 3.96 | 1.814 | −0.87 | 0.359 | −1.96 | 1250 | 2.25 | 1.659 | 0.42 | 13.711 | 2.65 |
| MS1b | 34.855 | 3.456 | 3.011 | 1.425 | 0.015 | 0.889 | 11.38 | 2.776 | −1.03 | 0.614 | −0.56 | 1420 | 1.38 | 1.888 | −0.64 | 14.583 | −0.32 |
| PS | 34.671 | 2.216 | 1.640 | 2.365 | 0.028 | 0.691 | 7.36 | 1.755 | −1.53 | 0.355 | −1.45 | 1300 | −2.39 | 2.067 | −3.06 | 15.472 | 3.72 |
| GS1[a] | 34.504 | 2.350 | 1.267 | 2.421 | 0.018 | 0.695 | 0.49 | 1.383 | −1.08 | 0.402 | −2.30 | 1660 | 9.05 | 0.771 | −3.71 | [b] | |
| GS2[a] | 34.642 | 2.519 | 1.571 | 2.314 | 0.026 | 0.592 | 16.10 | 1.653 | −0.30 | 0.339 | 7.71 | 1340 | 3.77 | 1.796 | −3.33 | 14.282 | 0.18 |
| BGN1H1 | 34.623 | 3.258 | 1.472 | 2.464 | 0.029 | 0.878 | −7.42 | 1.628 | 0.39 | 0.437 | −3.55 | 1670 | −2.08 | 1.504 | 0.56 | 12.901 | −1.96 |
| GNH3 | 34.648 | 2.664 | 2.194 | 2.304 | 0.0045 | 0.750 | 2.04 | 1.962 | 0.13 | 0.427 | 0.37 | 1410 | −0.04 | 1.713 | 0.38 | 14.203 | −0.28 |
| H1 | 34.564 | 2.595 | 1.845 | 1.897 | 0.0019 | 0.561 | 2.81 | 1.555 | −0.92 | 0.311 | −1.47 | 1320 | −1.46 | 1.488 | −1.45 | 12.861 | −0.03 |
| H2 | 34.617 | 2.775 | 1.855 | 1.858 | 0.0028 | 0.565 | 1.38 | 1.666 | −0.77 | 0.322 | −0.55 | 1280 | −1.29 | 1.623 | −0.82 | 13.479 | 0.29 |
| H3 | 34.646 | 2.787 | 1.951 | 1.901 | 0.0070 | 0.564 | 7.05 | 1.788 | −0.79 | 0.343 | 1.07 | 1290 | −0.88 | 1.702 | −1.18 | 13.840 | 0.31 |
| H4 | 34.669 | 2.909 | 2.246 | 2.144 | 0.0028 | 0.685 | 4.52 | 2.032 | −0.85 | 0.428 | −1.01 | 1400 | −1.28 | 1.729 | −1.18 | 13.759 | 1.45 |
| H5 | 34.609 | 2.793 | 1.974 | 1.915 | 0.0050 | 0.596 | 1.65 | 1.727 | −1.00 | 0.347 | −0.82 | 1340 | −1.55 | 1.615 | −1.31 | 13.385 | 0.40 |
| H6[a] | 34.593 | 2.637 | 2.121 | 2.064 | 0.0087 | 0.598 | 11.71 | 1.778 | 0.07 | 0.346 | 8.65 | 1310 | 5.33 | 1.623 | −2.19 | 13.501 | 0.09 |
| H7 | 34.559 | 2.621 | 2.048 | 2.006 | 0.0046 | 0.630 | 1.82 | 1.683 | −1.12 | 0.357 | −0.57 | 1410 | −1.52 | 1.527 | −2.33 | 12.992 | 0.23 |
| PCL2 | 34.507 | 2.554 | 1.880 | 1.977 | 0.0069 | 0.600 | 1.74 | 1.482 | −0.79 | 0.326 | −2.25 | 1440 | −1.87 | 1.291 | −3.27 | 11.761 | −1.15 |
| ALF1 | 34.055 | 2.013 | 3.389 | 2.033 | 0.040 | 0.565 | 18.59 | 1.495 | −0.53 | 0.386 | 3.52 | 1730 | 2.44 | 0.987 | −0.40 | 9.896 | −0.22 |
| ALF2 | 34.616 | 4.070 | 2.411 | 1.890 | 0.043 | 0.642 | 1.50 | 2.086 | −5.26 | 0.436 | −0.62 | 1440 | 1.01 | 1.638 | −6.94 | 13.188 | −3.66 |
| ALF3 | 34.283 | 2.883 | 2.653 | 1.952 | 0.017 | 0.565 | 11.29 | 1.473 | −0.06 | 0.358 | 2.46 | 1620 | 1.79 | 1.041 | 0.76 | 10.314 | −0.25 |
| ALF4 | 34.314 | 3.009 | 3.438 | 1.803 | 0.023 | 0.685 | 14.78 | 1.943 | −0.93 | 0.454 | 0.59 | 1590 | 0.52 | 1.297 | −2.38 | 11.667 | −1.20 |
| Mean error | | | | | | | 5.68 | | −0.72 | | 0.53 | | 0.43 | | −1.29 | | −0.20 |
| Standard deviation of error | | | | | | | 5.52 | | 0.96 | | 2.42 | | 2.25 | | 1.57 | | 1.27 |

[a]The tables for GS1, GS2, and H6 do not go up to the central density of the maximum-mass star. For most observables, the EOS can be safely extrapolated to higher density with minimal error. However, the maximum speed of sound is highly sensitive to how this extrapolation is done. Thus, we only use the maximum speed of sound up to the last tabulated point when comparing the values for the table and fit.

[b]GS1 has a maximum mass less than $1.4M_\odot$.


[1] L. Engvik *et al.*, Astrophys. J. **469**, 794 (1996).

[2] J. M. Lattimer and M. Prakash, Nucl. Phys. **A777**, 479 (2006).

[3] T. Klähn *et al.*, Phys. Rev. C **74**, 035802 (2006).

[4] D. Page and S. Reddy, Annu. Rev. Nucl. Part. Sci. **56**, 327 (2006).

[5] J. M. Lattimer and M. Prakash, Astrophys. J. **550**, 426 (2001).

[6] C. Vuille and J. Ipser, in *General Relativity and Relativistic Astrophysics*, edited by C. P. Burgess and R. C. Myers (American Institute of Physics, College Park Maryland, 1999), Vol. 493, p. 60.

[7] J. L. Zdunik, M. Bejger, P. Haensel, and E. Gourgoulhon, Astron. Astrophys. **450**, 747 (2006).

[8] M. Bejger, P. Haensel, and J. L. Zdunik, Mon. Not. R. Astron. Soc. **359**, 699 (2005).

[9] P. Haensel and A. Y. Potekhin, Astron. Astrophys. **428**, 191 (2004).
[10] M. Shibata, K. Taniguchi, and K. Uryu, Phys. Rev. D **71**, 084021 (2005).
[11] J. S. Read, C. Markakis, M. Shibata, K. Uryū, and J. Friedman (unpublished).
[12] B. D. Lackey, M. Nayyar, and B. J. Owen, Phys. Rev. D **73**, 024021 (2006).
[13] J. M. Lattimer and B. F. Schutz, Astrophys. J. **629**, 979 (2005).
[14] M. Bejger, T. Bulik, and P. Haensel, Mon. Not. R. Astron. Soc. **364**, 635 (2005).
[15] M. Prakash, T. L. Ainsworth, and J. M. Lattimer, Phys. Rev. Lett. **61**, 2518 (1988).
[16] F. Douchin and P. Haensel, Astron. Astrophys. **380**, 151 (2001).
[17] A. Akmal, V. R. Pandharipande, and D. G. Ravenhall, Phys. Rev. C **58**, 1804 (1998).
[18] B. Friedman and V. R. Pandharipande, Nucl. Phys. **A361**, 502 (1981).
[19] R. B. Wiringa, V. Fiks, and A. Fabrocini, Phys. Rev. C **38**, 1010 (1988).
[20] M. Baldo, I. Bombaci, and G. F. Burgio, Astron. Astrophys. **328**, 274 (1997).
[21] W. Zuo, I. Bombaci, and U. Lombardo, Phys. Rev. C **60**, 024605 (1999).
[22] H. Muther, M. Prakash, and T. L. Ainsworth, Phys. Lett. B **199**, 469 (1987).
[23] H. Müller and B. D. Serot, Nucl. Phys. **A606**, 508 (1996).
[24] V. R. Pandharipande and R. A. Smith, Nucl. Phys. **A237**, 507 (1975).
[25] N. K. Glendenning and J. Schaffner-Bielich, Phys. Rev. C **60**, 025803 (1999).
[26] S. Balberg and A. Gal, Nucl. Phys. **A625**, 435 (1997).
[27] N. K. Glendenning, Astrophys. J. **293**, 470 (1985).
[28] M. Prakash, J. R. Cooke, and J. M. Lattimer, Phys. Rev. D **52**, 661 (1995).
[29] M. Alford, M. Braby, M. Paris, and S. Reddy, Astrophys. J. **629**, 969 (2005).
[30] J. Negele and D. Vautherin, Nucl. Phys. **A207**, 298 (1973).
[31] N. K. Glendenning and C. Kettner, Astron. Astrophys. **353**, L9 (2000).
[32] J. M. Lattimer and M. Prakash, Phys. Rep. **442**, 109 (2007).
[33] S. M. Ransom *et al.*, Science **307**, 892 (2005).
[34] P. C. C. Freire, A. Wolszczan, M. van den Berg, and J. W. T. Hessels, Astrophys. J. **679**, 1433 (2008).
[35] D. J. Champion *et al.*, Science **320**, 1309 (2008).
[36] J. P. W. Verbiest *et al.*, Astrophys. J. **679**, 675 (2008).
[37] P. C. C. Freire *et al.*, Astrophys. J. **675**, 670 (2008).
[38] P. Haensel, J. Zdunik, and F. Douchin, Astron. Astrophys. **385**, 301 (2002).
[39] J. Cottam, F. Paerels, and M. Mendez, Nature (London) **420**, 51 (2002).
[40] J. Cottam *et al.*, Astrophys. J. **672**, 504 (2008).
[41] F. Özel, Nature (London) **441**, 1115 (2006).
[42] J. W. T. Hessels *et al.*, Science **311**, 1901 (2006).
[43] P. Kaaret *et al.*, Astrophys. J. **657**, L97 (2007).
[44] N. Stergioulas, S. Koranda, and J. Friedman, Astrophys. J. **488**, 301 (2002).
[45] N. Glendenning, Phys. Rev. D **46**, 4161 (1992).
[46] N. Stergioulas, http://www.gravity.phys.uwm.edu/rns.
[47] P. Haensel and J. L. Zdunik, Nature (London) **340**, 617 (1989).
[48] P. Haensel, M. Salgado, and S. Bonazzola, Astron. Astrophys. **296**, 745 (1995).
[49] J. L. Friedman, L. Parker, and J. R. Ipser, Astrophys. J. **304**, 115 (1986).
[50] J. M. Lattimer, M. Prakash, D. Masak, and A. Yahil, Astrophys. J. **355**, 241 (1990).
[51] G. B. Cook, S. L. Shapiro, and S. A. Teukolsky, Astrophys. J. **424**, 823 (1994).
[52] J. M. Lattimer and B. F. Schutz, Astrophys. J. **629**, 979 (2005).
[53] I. A. Morrison, T. W. Baumgarte, S. L. Shapiro, and V. R. Pandharipande, Astrophys. J. **617**, L135 (2004).
[54] F. Özel, T. Guver, and D. Psaltis, Astrophys. J. **693**, 1775 (2009).
[55] T. Guver, F. Özel, A. Cabrera-Lavers, and P. Wroblewski, arXiv:0811.3979.
[56] É. É. Flanagan and T. Hinderer, Phys. Rev. D **77**, 021502 (2008).
[57] J. B. Hartle, Astrophys. J. **150**, 1005 (1967).
[58] L. Lindblom, Astrophys. J. **398**, 569 (1992).
[59] J. L. Friedman, J. R. Ipser, and R. D. Sorkin, Astrophys. J. **325**, 722 (1988).
[60] G. Cook, S. Shapiro, and S. Teukolsky, Astrophys. J. **424**, 823 (1994).